

# Counts-in-Cells of subhalos in the Illustris-TNG simulations: the role of baryonic physics

Christine C. Dantas<sup>1\*</sup>

<sup>1</sup>*Divisão de Astrofísica (INPE-MCTI), São José dos Campos, 12227-010, SP, Brazil*

Accepted XXX. Received YYY; in original form 19 June 2022

## ABSTRACT

We present an analysis of the Counts-in-Cells (CiC) statistics of subhalos in the publicly available Illustris-TNG cosmological simulations (TNG100-1, TNG100-3 and TNG300-3), in redshifts ranging from  $z = 0$  to  $z = 5$ . We fit the CiC statistics to two models: the gravitational quasi-equilibrium distribution (GQED) and the negative binomial distribution (NBD). We analyzed differences between “full” runs and their associated “dark-only” counterparts, in terms of GQED and NBD, and also by the use of gaussian kernel density estimates. We discuss the behaviour of the best-fit parameters  $\bar{N}$  (average number of subhalos per cell), and the clustering parameters  $b$  (GQED) and  $g$  (NBD), in terms of redshifts and comoving cell sizes. We found that “full” and “dark-only” TNG runs follow similar CiC distributions. However, there are quantifiable distinctions between these sets of runs in the evolution and scaling of the best-fit parameters. We compare our results with previous numerical, observational and “mock” catalogs, and found similar scaling and evolutionary trends in all samples, up to factors in the amplitude of parameter values, possibly regulated by different magnitude cutoffs in the observational samples. Our results suggest the overall validity of the GQED and NBD models for describing the large-scale statistics of extended, multi-component gravitational systems and subject to complex baryonic physics. Our analysis indicate that gravithermodynamics is generally suitable for describing gravitational clustering in the presence of baryonic physics and, with proper refinements, it may provide additional theoretical guidance for the modelling of bias.

**Key words:** large-scale structure of Universe; galaxies: clusters: general; galaxies: groups: general; dark matter

## 1 INTRODUCTION

The recognition that the Universe contains large-scale structures involved a long process of discovery, from initial speculations to physical theories, guided by increasingly refined data from observational surveys (see a historical account in, e.g., [Saslaw 2000](#)). These structures, composed of smaller gravitational units (clusters of galaxies, galaxies, etc), probably formed from small initial fluctuations in the early Universe, and evolved through gravitational instability in an expanding space-time. Observations such as the cosmic microwave background radiation and baryon acoustic oscillation signals ([Planck Collaboration et al. 2016](#)), high-redshift Type Ia supernovae ([Riess et al. 1998](#); [Perlmutter et al. 1999](#)), etc, converged to a spatially flat  $\Lambda$ CDM cosmological model, which however has recently been under significant tension due to revealing inconsistencies (e.g. [Garcia-Quintero et al. 2019](#)).

Our current understanding indicates that galaxies (and other observables such as quasars, line intensities maps, diffuse backgrounds, etc) are only tracers of the large-scale structures, with the mass component being dominated by dark matter (DM), evolving in an accelerated expanding background (due to some form of “dark energy”). In this  $\Lambda$ CDM cosmology, large-scale structures are formed hierarchically, in which dark matter halos are assembled from the merging of smaller structures. The relation between the distribution of tracers and the underlying distribution of (total) matter, termed “bias” ([Weinberg](#)

\* E-mail: christine.dantas@inpe.br

et al. 2004; Desjacques et al. 2018), its nature and how it evolves in time, is of fundamental importance, not only for the understanding and characterization of large-scale structures, but also as tests for cosmological models. Furthermore, bias manifests in the clustering of halos themselves, which depends not only on halo mass (more massive haloes are more clustered than less massive ones), but also on the halo assembly history (at fixed mass, haloes with lower mass that assemble earlier are more clustered than haloes assembling at later times) and other secondary properties (e.g. Croton et al. 2007; Montero-Dorta et al. 2020, and references therein).

Several approaches have been developed in modelling bias, such as in the semi-analytic models (SAMs, e.g. Baugh 2006), the empirical halo occupation distribution model (e.g. Berlind & Weinberg 2002), and the galaxy-subhalo correspondence model, combined with the abundance matching method (e.g. Kim et al. 2008; Trujillo-Gomez et al. 2011, and references therein). Although these models achieve good results in terms of reproducing observables, they often require the tuning of parameters and further investigations, specially made in combination with computationally expensive hydrodynamical simulations. On the other hand, the study of large-scale structures and its nonlinear evolution also relies on statistical tools such as the power spectra and correlation functions (Peebles 1980; Bernardeau et al. 2002). Another approach is given by the Counts-in-Cells (CiC) probability distribution function (PDF) (Saslaw 1985, 2000), in which discrete objects such as galaxies are counted inside cells of fixed size and shape in an ensemble. The CiC can also be expressed as an appropriately smoothed “density in spheres” distribution, and it can be derived from fundamental theories of gravitational clustering and/or estimated from survey data (e.g. Uhlemann et al. 2018).

The gravitational quasi-equilibrium distribution (GQED) is a prediction for the form of the CiC PDF for the gravitational evolution of discrete bound systems, such as galaxies in large-scale structures, in an expanding Universe. The GQD was first derived by Saslaw & Hamilton (1984), leading to several subsequent studies and refinements (summarized in the book by Saslaw 2000, following an earlier foundational exposition in Saslaw 1985). In GQED, the pairwise properties of the gravitational potential are consistently introduced into a gravithermodynamical theory, under certain hypotheses, but it has also been subsequently derived from statistical mechanics principles by Ahmad et al. (2002). Another CiC PDF is the negative binomial distribution (NBD), first proposed in a cosmological context by Carruthers & Duong-van (1983), and subsequently explored in Elizalde & Gaztanaga (1992) (see also, e.g. Yang & Saslaw 2011; Hurtado-Gil et al. 2017; Wen et al. 2020). Note that the NBD model has been shown to be unphysical Saslaw & Fang (1996), even though it does provide a good fit to the observed CiC PDFs (e.g. Hurtado-Gil et al. 2017); therefore, it can be used as a provisional approximation for an underlying CiC PDF, yet to be derived from theory.

Predictions for the CiC PDF are hindered by nontrivial issues, such as galaxy bias, inherent difficulties related to nonlinear gravitational dynamics, redshift-space distortions, numerical costs and artifacts, etc. However, recent investigations have produced an ample literature with increasingly accurate models (see, e.g. Uhlemann et al. 2018, and references therein). For example, in Uhlemann et al. (2018), a bias model leads to precise predictions for a parametrized densities-in-cells statistics of mass tracers. Their model was validated on statistical measurements of subhalo densities in the  $\Lambda$ CDM cosmological N-body, 3.15 Gpc  $h^{-1}$  box, Horizon Run 4 simulation (Kim et al. 2015). Recently, Wen et al. (2020) used the 648 Mpc  $h^{-1}$  box, Dark Energy Universe Simulations (DEUS, Alimi et al. 2012) to study the CiC PDFs of halos, as a function of scale and redshift, finding features which could be used to observationally distinguish between different dark energy cosmologies.

The Illustris The Next Generation (TNG) project<sup>1</sup> presents a prominent series cosmological simulations (Nelson et al. 2019; Pillepich et al. 2018; Springel et al. 2018; Nelson et al. 2018; Naiman et al. 2018; Marinacci et al. 2018), suitable for the study of galaxy formation and evolution, which incorporates a wide range of physical processes and SAMs, following the coupled dynamics of baryons and DM through a state-of-the-art magnetohydrodynamical numerical code (AREPO, Springel 2010). “Dark-only” counterparts to the “full” runs are also available. There are several studies concerning the large-scale clustering and bias using the Illustris-TNG simulations (e.g. Springel et al. 2018; Martizzi et al. 2019, 2020; Montero-Dorta et al. 2020). Springel et al. (2018) investigated bias in terms of correlation functions and power spectra of various components of TNG simulations. They analyzed the clustering of subhalos in terms of scale and redshifts in the largest simulation box, the TNG300 runs, finding that bias depends on the type of tracer and scale. The two-point correlation function of the simulated galaxies shows significant agreement with observational data at  $z \sim 0.1$  (Li & White 2009), based on the Sloan Digital Sky Survey (SDSS) (SDSS Abazajian et al. 2009, DR7).

In the present work, we investigate the CiC probability distribution functions (PDFs) in the publicly available Illustris TNG simulations (TNG100-1, TNG100-3 and TNG300-3). We fit the CiC PDF to the GQED and the NBD models, and also obtain their gaussian kernel density estimates, in which we analyze potential differences between “full” runs and their “dark-only” counterparts. Our paper is organized as follows: in Sec. 2, we present the methodology used: the selection of TNG runs, a summary of the CiC methods used to extract the CiC statistics from the simulations, the GQED and NBD models and the fitting procedure. In Sec. 3, we present our results: a qualitative description of the obtained CiC PDFs, a quantitative analysis of the GQED and NBD best-fit parameters and kernel density estimates. In Sec. 4, we summarize and discuss our

<sup>1</sup> <https://www.tng-project.org/>

results. The Appendices provide brief studies on the behaviour of cell sampling and residues. The cosmology parameters used in the present paper are those defined in the Illustris-TNG simulations, namely:  $\Omega_{\Lambda,0} = 0.6911$ ,  $\Omega_{m,0} = \Omega_{DM,0} + \Omega_{b,0} = 0.3089$ ,  $\Omega_{b,0} = 0.0486$ ,  $\sigma_8 = 0.8159$ ,  $n_s = 0.9667$  and  $h = 0.6774$  (Planck Collaboration 2016).

## 2 METHODOLOGY

Our motivation is to obtain the CiC statistics for the “full” and “dark-only” Illustris-TNG simulations, to evaluate the quality of the fits, and to look for potential differences in the large-scale clustering between both sets of simulations, including the behaviour of parameters of interest across cosmological timescales. In this section, we describe the selection of the TNG-Illustris simulations and the extraction of subhalos’ data for our analysis, including a brief description of the studied models and the applied methodology for the CiC computations.

The currently publically available simulations are the TNG300 and TNG100 runs, each with three levels of resolution. These simulations have sizes of:  $L_{SIM}(\text{TNG100}) = 75 \text{ [Mpc h}^{-1}]$ ;  $L_{SIM}(\text{TNG300}) = 205 \text{ [Mpc h}^{-1}]$ . The smaller volume in the series, TNG50, is not available yet, by the time of the present writing. The higher resolution run is denoted by the complementary digit “-1” (i.e., “TNG300-1”), with lower-resolution counterparts with increasing digits for lower resolutions (i.e., “TNG300-3” for the lowest resolution run of TNG300). “Dark-matter only” counterparts for each of the “full” TNG300 and TNG100 simulations are also available at each of the three resolution levels. For reference, we mention briefly the number of particles,  $N_{DM}$ , and mass resolution of DM particles,  $m_{DM}$  (in  $M_{\odot}$ ), for the TNG simulations used in our work (c.f. Sec. 2.1): TNG100-1:  $N_{DM} = 1820^3$ ,  $m_{DM} = 7.5 \times 10^6$ ; TNG100-3:  $N_{DM} = 455^3$ ,  $m_{DM} = 4.8 \times 10^8$ ; TNG300-3:  $N_{DM} = 625^3$ ,  $m_{DM} = 3.8 \times 10^9$ . The respective “dark-only” counterparts have the same  $N_{DM}$ , and slightly lower mass resolutions<sup>2</sup>.

The TNG300 runs are more adequate for the statistical analysis of large-scale galaxy clustering. The TNG100 runs follow the same initial conditions (with updated cosmological parameters) of its predecessor, the “Illustris” simulation, with volume and resolution lying between the TNG300 and the TNG50 simulations. Hence, the TNG100 is adequate for the study of clustering of at scale of intermediate mass subhalos. The TNG300 is more adequate than the TNG100 for the applicability of the gravitational quasi-equilibrium theory (GQED Saslaw 2000), which relies on a gravithermodynamical approach for the description of clustering in the largest structures in the Universe. Nevertheless, we are also interested in analyzing the adequacy of the CiC models at the intermediate scale of the TNG100, in order to learn how a smaller volume size influences the results. However, we did not cover in the evolution of parameters in redshift as finely for the TNG100 as we did for the TNG300. In the next subsections, we describe in more detail our selections and applied methods.

### 2.1 Selection of the Illustris-TNG runs for the CiC statistics

We performed a preliminary evaluation to determine the number of CiC computations suitable for our project, given constraints regarding our computational resources and timeframe. We first analyzed the lowest resolution run, TNG100-3, at  $z = 0$ . For the CiC computations, we developed a Python (2019) code to implement two methods, given in Itoh et al. (1988) (hereon, [IIS88]) and Leicht et al. (2019) (hereon, [Lei19]; details of these methods are presented in the next section). Based on that first evaluation, we established a grid of runs considering the lowest resolution versions of the both available volumes, namely, the TNG100-3 and TNG300-3 (both “full” and “dark-only” runs).

In Tab. 1 we present our grid, resulting in a total of 136 CiC computations. In Fig. 1, we present the comoving simulation boxes (“full runs”) of the TNG100-3 and TNG300-3 at redshifts  $z = 0$  and  $z = 5$ . Note that the comoving number of available subhalos, understood as gravitationally bound structures identified by the SUBFIND algorithm (Nelson et al. 2019), decreases for higher redshifts (c.f. Fig. 1 and the column on the number of subhalos, “ $N_{sh}$ ”, in Tab. 1). The columns “CiC Method”, “Cell Radii”, number of subhalos (“ $N_{sh}$ ”) and number of excluded subhalos (“ $N_{excl}$ ”) in Tab. 1 are explained in more detail Sec. 2.2.

We cover a range of redshifts for the TNG300-3, namely  $z = \{0.00, 0.05, 0.11, 1.00, 2.00, 3.01, 4.01, 5.00\}$ , but only  $z = \{0.00, 5.00\}$  for the TNG100-3 runs (c.f. Tab. 1). The respective “dark-only” counterparts were analyzed with the same corresponding redshift ranges, comoving cell radii, and methodology. We also list two other specific studies. First, a single run, denoted “TNG300-3-H”, providing a reference study for a case in which we used a larger number of CiC cells, as explained in Sec. 2.2.2 and discussed in more detail in the App. A. We also analyzed the highest simulation run of the 100 Mpc volume, the TNG100-1, but the selection of subhalos differs from all other cases. We label this simulation as “100-1-Mock” in Tab 1; details for this case are given in Sec. 2.2.3.

<sup>2</sup> For complete information, please refer to the Illustris-TNG project site.

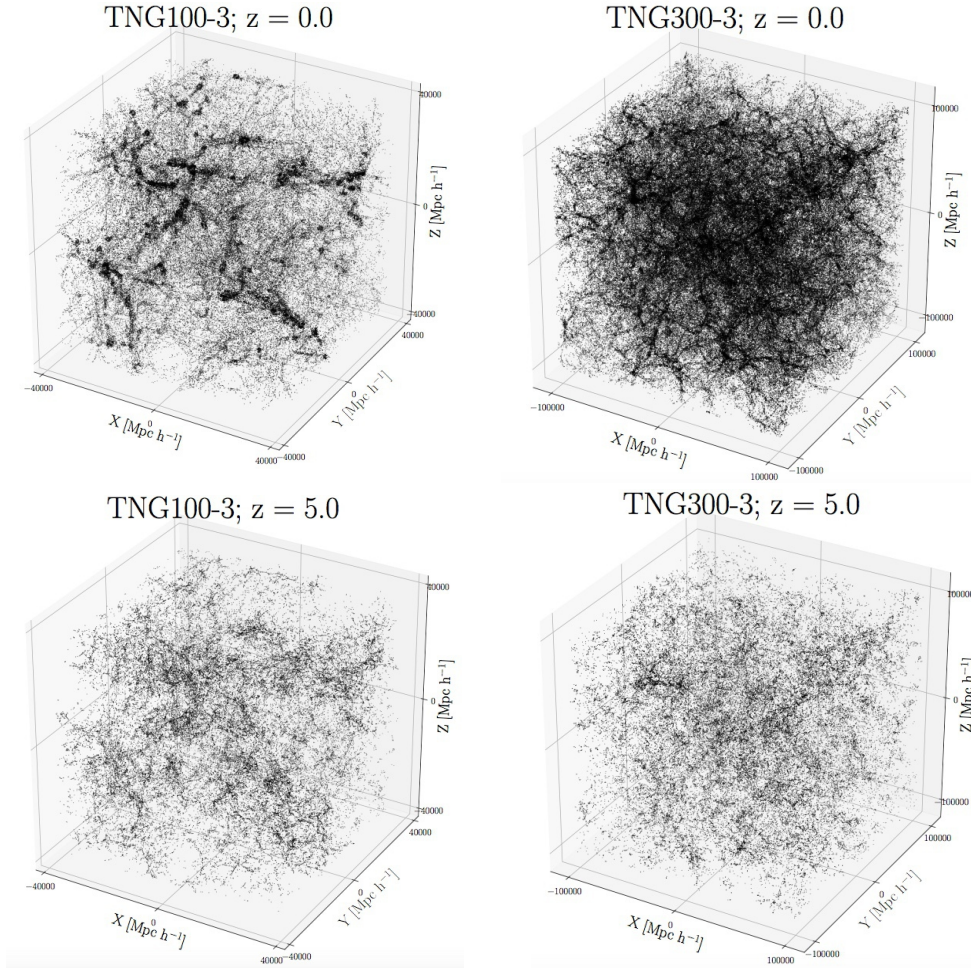


**Figure 1.** Comoving simulation boxes (“full” runs) with (centered) coordinates of the TNG100-3 (left) and TNG300-3 (right) at redshifts  $z = 0$  (top) and  $z = 5$  (bottom). Each dot represents the spatial position of the particle with the minimum gravitational potential energy of each subhalo. Note that TNG100 and TNG300 are not shown in the same scale.

## 2.2 CiC Methods

### 2.2.1 An overview of two methods

The CiC statistics is generally obtained from an ensemble of cells with a certain form and size, in which the number of a given class of objects is counted within each cell. In the present case, the objects are the Illustris-TNG “subhalos” and the cells are chosen from different sets of comoving spherical cells. The CiC statistics then reflects the underlying probability distribution function (PDF),  $f_V(N)$ , of the number of objects per cell volume  $V$ , between  $N$  and  $N + dN$ . The interval or bin  $dN$  should be chosen to produce a “smooth” enough PDF, and this depends on the data size (c.f. Sec. 2.3, final paragraph). Here we use the terms “CiC statistics”, “CiC PDFs” and “ $f_V(N)$ ” interchangeably.

We considered two methods for obtaining the CiC statistics, given by Itoh et al. (1988) [IIS88] and Leicht et al. (2019) [Lei19], which we label as “Rand-method” and “Grid-method”, respectively. The main difference between these methods is the following.

*The “Rand-method”.* This method is explained in [IIS88], an early numerical investigation about the adequacy of the GQED for describing of the gravitational N-body clustering of 4000 point particles (each representing a galaxy), evolving in an expanding universe (represented by a sphere of comoving unity radius). The gravitational interaction of these particles was followed in comoving coordinates, for different cosmological models (total mass density parameter given by  $\Omega_0 = \{0.01, 0.1, 1.0\}$ , with “cold” and “warm” initial velocity distributions). The CiC method in [IIS88] consisted of randomly generating 9500 points within a “selection sphere” at the center of the simulation box. This procedure was repeated for each investigated configuration (i.e., for each “snapshot” at certain scale factors of interest). The radius of this “selection sphere” depended on the cell radius for the counting procedure. [IIS88] used selection spheres of radii  $R = \{0.8, 0.7, 0.6, 0.6\}$  for corresponding cell radii given by

**Table 1.** Summary of the analyzed simulations

Simulation (TNG) (1)	Redshift (2)	CiC Method (3)	Cell Radii [Mpc $h^{-1}$ ] (4)	$N_{\text{sh}}$ (5)	$N_{\text{excl}}$ (6)
300-3	0.00	“Rand” [IIS88]	$\mathcal{R}_a = \{10.25, 20.5, 30.75, 41.0\}$ , $\mathcal{R}_b = \{6.0, 12.0, 24.0\}$	391144	23535
300-3	0.05	“Rand”	$\mathcal{R}_a$ , $\mathcal{R}_b$	396402	23574
300-3	0.11	“Rand”	$\mathcal{R}_a$ , $\mathcal{R}_b$	399948	23633
300-3	1.00	“Rand”	$\mathcal{R}_a$ , $\mathcal{R}_b$	429194	20056
300-3	2.00	“Rand”	$\mathcal{R}_a$ , $\mathcal{R}_b$	384814	11091
300-3	3.01	“Rand”	$\mathcal{R}_a$ , $\mathcal{R}_b$	271945	4425
300-3	4.01	“Rand”	$\mathcal{R}_a$ , $\mathcal{R}_b$	156950	1233
300-3	5.00	“Rand”	$\mathcal{R}_a$ , $\mathcal{R}_b$	72591	248
300-3-Dark	0.00	“Rand”	$\mathcal{R}_a$ , $\mathcal{R}_b$	372177	26627
300-3-Dark	0.05	“Rand”	$\mathcal{R}_a$ , $\mathcal{R}_b$	373988	26693
300-3-Dark	0.11	“Rand”	$\mathcal{R}_a$ , $\mathcal{R}_b$	375860	26719
300-3-Dark	1.00	“Rand”	$\mathcal{R}_a$ , $\mathcal{R}_b$	374473	22318
300-3-Dark	2.00	“Rand”	$\mathcal{R}_a$ , $\mathcal{R}_b$	307526	12253
300-3-Dark	3.01	“Rand”	$\mathcal{R}_a$ , $\mathcal{R}_b$	202685	4879
300-3-Dark	4.01	“Rand”	$\mathcal{R}_a$ , $\mathcal{R}_b$	108238	1372
300-3-Dark	5.00	“Rand”	$\mathcal{R}_a$ , $\mathcal{R}_b$	47491	293
300-3-H	0.00	“Rand” (*)	$\mathcal{R}_b$	391144	23535
100-3	0.00	“Grid” [Lei19]	10.00, 11.25	118820	2221
100-3	0.00	“Rand”	$\mathcal{R}'_a = \{3.75, 7.5, 11.25, 15.0\}$	118820	2221
100-3	5.00	“Rand”	$\mathcal{R}'_a$	68031	34
100-3-Dark	0.00	“Rand”	$\mathcal{R}'_a$	116020	2333
100-3-Dark	5.00	“Rand”	$\mathcal{R}'_a$	45700	36
100-1-Mock	0.00	“Grid”	10.00	4371211	4359784
100-1-Mock	0.00	“Rand”	$\mathcal{R}'_a$	4371211	4359784

Columns: (1) simulation label; (2) redshift at which the CiC was applied; (3) applied CiC method (c.f. Secs. 2.2.1 and 2.2.2); (4) cell radii used for the applied CiC method (c.f. Sec. 2.2.3); (5) total number of candidate subhalos ( $N_{\text{sh}}$ ); and (6) number of excluded subhalos ( $N_{\text{excl}}$ ; c.f. Sec. 2.2.3). The number of cells for the largest selection sphere is 9500 for the “Rand”-method, which was doubled (highlighted with “\*”) in the 300-3-H CiC computation. For the “Grid”-method, a regular grid of 216000 cells was used.

$r = \{0.1, 0.2, 0.3, 0.4\}$ , in which each cell was centered on the randomly generated points. The selection spheres were adopted to avoid boundary effects and to include a sufficient number of particles for the CiC statistics. In other words, a pair  $(R_i, r_i)$  defines the selection sphere and cell radius for each computation of  $f_V(N)$ , where  $V \equiv V_i$  refers to the cell volume with radius  $r_i$ .

*The “Grid-method”.* In [Lei19], a CiC statistics was obtained for the Illustris TNG100 simulation in the context of 21 cm intensity mapping of neutral hydrogen. The CiC provided a statistics on the mean matter densities of neutral hydrogen, matter, and mass-weighted haloes, in overlapping spheres of comoving radius of  $R = 5$  Mpc  $h^{-1}$ , centered on a regular  $128^3$  grid. This produced  $\sim 2$  million density samples, in a redshift range of  $z = 1$  to 5. Their fixed choice of  $R$  was determined as a compromise between a sufficiently large cell radius and at the same time a large number of independent cells (hence a small enough cell size) for a satisfactory statistics (see Sec. 2 in [Lei19] for details).

### 2.2.2 Choice of CiC method

We performed a preliminary evaluation of the CiC methods described in the previous subsection, through an implementation of a series of Python (2019) codes that extract the TNG subhalo data and compute the corresponding counting procedures. Our initial evaluation considered only the medium-sized, lowest resolution run, TNG100-3, at  $z = 0$ . We considered a coarser grid than that in [Lei19] due to our computational constraints, i.e., we used a regular  $60^3 = 216000$  grid, imposing an exclusion margin of 750 kpc to avoid boundary effects. For this preliminary test, we considered two counting cell radii: 10 [Mpc  $h^{-1}$ ] and 11.25 [Mpc  $h^{-1}$ ]. For the “Rand”-method, we used the same number of cells (9500) within the “selection sphere”, applied to the preliminary CiC computations for the TNG100-3 at  $z = 0$ . Both CiC methods resulted in qualitatively similar outcomes. Computations using both these methods were also performed for the “TNG-100-1-Mock”. The results of these preliminary tests are discussed in detail in Sec. 3, together with the full results.

Given the similarity of the results in both CiC methods, we fixed our full, subsequent analysis to the “Rand”-method. We

used the same CiC parameters as in [IIS88], including the same number (9500) of random cell centers for both the TNG100-3 and TNG300-3. This choice, however, could introduce a less satisfactory statistics for the TNG300-3 runs. A brief study in this regard was made using the “full” TNG300-3 run with the double of counting cells, denoted “TNG300-3-H” in Tab 1. More details can be found in the App. A.

### 2.2.3 Comoving cell sizes and proxies for galaxies

Following the “Rand”-method, comoving cell radii were defined as fractions of the simulation size. The “selection sphere” for the valid inclusion of random cell centers depends on the cell size, as explained previously (Sec. 2.2.1). We summarize two sets cell radii that we used, as follows:

(i) *The  $\mathcal{R}_a$ -set*: comoving cell radii as fixed fractions of the simulation size (“Rand-method” [IIS88]). We defined a set of cell radii given by:  $\mathcal{R}_a = \{0.1, 0.2, 0.3, 0.4\} \times R_{SIM}$  [Mpc  $h^{-1}$ ], with  $R_{SIM} = L_{SIM}/2$ . Each cell center in set  $\mathcal{R}_a$  must be inside a selection radius given, respectively, by:  $R_{sph} = \{0.8, 0.7, 0.6, 0.6\} \times R_{SIM}$  [Mpc  $h^{-1}$ ], to avoid boundary effects. This gives different comoving cell sizes for the TNG300-3 and TNG100-3 runs, namely: for TNG300-3,  $\mathcal{R}_a = \{10.25, 20.5, 30.75, 41.0\}$  [Mpc  $h^{-1}$ ]; and for TNG100-3,  $\mathcal{R}'_a = \{3.75, 7.5, 11.25, 15.0\}$  [Mpc  $h^{-1}$ ].

(ii) *The  $\mathcal{R}_b$ -set*: comoving cell radii of  $\mathcal{R}_b = \{6.0, 12.0, 24.0\}$  [Mpc  $h^{-1}$ ]. This set was only analyzed for the TNG300-3 simulations. This choice of radii is the same as that explored in Yang & Saslaw (2011). The respective selection radii were defined as:  $R_{sph} = \{0.8, 0.7, 0.6\} \times R_{SIM}$  [Mpc  $h^{-1}$ ].

We used the SUBFIND object catalogue (c.f. Pillepich et al. 2018, and references therein) for the identification of subhalos the counting procedure. Hence, subhaloes were taken as proxies for “galaxy-like”, bound objects, that is, any bound structure detected by the SUBFIND algorithm was included, depending on the criteria below. Hence, our selection might include subhalos without significant luminous particles in the “full” runs, or subhalos with internal subhalos, if they meet those criteria. We do not differentiate between “central” and “satellite” galaxies (Pillepich et al. 2018). For the “dark-only” simulations, we used the same criteria as below. The overall matching between bound structures in the SUBFIND catalog in both “full” and “dark-only” runs is the basis for a direct comparison between their corresponding CiC statistics results. Hence, for the counting procedure, we selected subhaloes with attributes restricted to the following criteria:

- Subhalo mass range: subhalos must have a minimum mass of  $2.5 \times 10^8 [M_\odot h^{-1}]$  (as in [Lei19]), and a maximum cutoff mass of  $\sim 10^{13} [M_\odot h^{-1}]$ .
- Subhalo attribute ‘SubhaloFlag’ must be equal to 1 (indicating that the particles composing the subhalo have a cosmic origin).

In Tab. 1, we quote in columns (5) and (6) the total number of initial candidate subhalos ( $N_{sh}$ ) and the number of excluded subhalos ( $N_{excl}$ ) after applying the criteria above. In App. A, we present graphically the behaviour of the final number of subhalos (namely,  $N_{sh} - N_{excl}$ ), compared with the sampled subhalos obtained in the CiC procedure, that is, the resulting ensemble of cells generating the CiC statistics, as function of redshift and cell size. A discussion on the quality of the CiC statistics is given in that appendice.

As mentioned previously, we used a different criteria for galaxy proxies for the TNG-100-1 simulation, which was based on the publically available “mock” catalog by Rodriguez-Gomez et al. (2019) (“TNG-100-1-Mock”). In this case, for selecting admissible subhalos, we matched the individual subhalo ID’s listed in that catalog to those in the SUBFIND catalog of the TNG100-1 at  $z = 0$ . The “mock” catalog includes subhalos with (total) stellar mass greater than  $10^{9.5} M_\odot$  and tailored to the Sloan Digital Sky Survey (SDSS York et al. 2000), as explained in Rodriguez-Gomez et al. (2019). Furthermore, we cut magnitudes in the  $r$ -band for synthetic objects fainter than 17.77 mag, resulting in 11427 subhalos, representing “galaxies” as would be observed in that band at  $z \lesssim 0.05$ .

## 2.3 Models and fitting procedure

We study two models for the CiC statistics: the gravitational quasi-equilibrium distribution (GQED) and the negative binomial distribution (NBD). Both are related to the Poisson distribution: the former is a Poisson-sampled, truncated Borel distribution, and the latter is a Poisson-sampled, Gamma distribution (Wen et al. 2020, and references therein). GQED is motivated by a gravithermodynamical theory; whereas the NBD was initially introduced in cosmology without an underlying physical foundation by Carruthers & Duong-van (1983), as a good approximation to the distribution of Zwicky clusters, and further developed by Elizalde & Gaztanaga (1992).

The gravithermodynamical theory leading to the GQED assumes that the galaxy clustering evolves through a series of quasi-equilibrium states due to a cancelling effect of the long range, mean gravitational field from the expansion of the universe

(Saslaw 2000). The resulting distribution function,  $f_V(N) \equiv f_{\text{GQED}}(N)$ , representing the probability that a cell of volume  $V$  of arbitrary shape contains  $N$  galaxies, has a form which modifies a Poisson PDF due to the presence of correlations:

$$f_{\text{GQED}}(N) = \frac{\bar{N}(1-b)}{N!} [\bar{N}(1-b) + Nb]^{N-1} \exp[-\bar{N}(1-b) - Nb], \quad (1)$$

where  $\bar{N} = nV$  is the expected average number of galaxies in the given volume  $V$ , with average density  $n$ . The aggregation or clustering parameter  $b$  is related to the degree of clustering of galaxies at a certain state, and represents the average departure from a noninteracting ensemble of cells of a given volume at that state. A more detailed physical interpretation for this parameter, in terms of the average density and kinetic temperature  $T$  of the system, was explored in subsequent developments (e.g., Saslaw & Fang 1996; Ahmad et al. 2002).

For a completely noninteracting system (behaving like a perfect gas), one obtains the lower limit  $b = 0$ , retrieving the Poisson PDF. The case  $N = 0$  represents the distribution of empty voids. The upper limit  $b \rightarrow 1$  can be understood in the following way. The clustering parameter  $b$  can be expressed similarly in form to the virial ratio ( $b = -W/2K$ ; see Eq. 2 below), but it actually represents an ensemble average ratio of the gravitational *correlation* energy ( $W$ ) to twice the kinetic energy ( $K$ ) of the *peculiar velocities* of galaxies in an *infinite* universe. The usual virial ratio is only meaningful for finite, bound systems, and not in the gravithermodynamics of infinite systems as in the case of the GQED theory. However, the limit  $b \rightarrow 1$  represents a state in which the entire universe would be hierarchically virialized into a single bound unit, in which both virial descriptions would become equivalent. However, this latter, limiting state is not physically meaningful.

Numerical studies of the gravitational clustering of galaxies in a range of expanding universe models have shown that structures quickly relax to the GQED form of Eq. 1, and that they subsequently evolve, in general, through a series of quasi-equilibrium states (e.g. Itoh et al. 1988, 1993; Wen et al. 2020). Each of such states would satisfy Eq. 1 for a given value of  $b$ , in other words, the theory admits a time-dependent  $b(t)$ , which increases slowly from a lower value, as clustering proceeds hierarchically into larger and larger scales with time (Saslaw 1986, 2000).

It is also important to understand how the value of  $b$  depends on the counting cell size (Saslaw & Crane 1991; Sheth & Saslaw 1996), and how correlations evolve more rapidly depending on the spatial scale, as nonlinear structures develop first from near-neighbour interactions on smaller scales than in larger ones. This effect is explicitly encoded in the expression for  $b$  in terms of the two-point correlation function  $\xi$  (e.g., Saslaw & Hamilton 1984; Saslaw & Crane 1991; Saslaw 2000):

$$b = -\frac{W}{2K} = \frac{2\pi Gm^2n}{3T} \int_0^\infty \xi(n, T, r) r dr, \quad (2)$$

where  $m$  is the average galaxy mass. Depending on the initial conditions of the Universe, there could be a characteristic scale at which the correlation function would not contribute to the integral in Eq. 2, leading to  $b \rightarrow 0$ , above such uncorrelated, large scales. This would be the case of an initial Poissonian distribution. For very small scales, with either one or zero galaxies, the distribution function would also tend to Poissonian one (Saslaw & Crane 1991; Saslaw 2000).

It is important to understand such limiting behaviours as they clearly show interesting information on how the gravitational clustering proceeds directly in terms of spatial regions. For instance, in smaller scales, it is fundamental to search for the effects of mergers on the predictions of the CiC statistics, and on larger scales, indications of non-Poissonian initial conditions. Other important effects to be understood in terms of predictions for the CiC statistics are the role of the dominant dynamical component (DM), specially whether it is individually associated with galaxies through distinct haloes, or more uniformly distributed throughout space, as well as the effects of baryon dissipation in the overall dynamics. Percentage differences in the distribution functions for different dark energy cosmologies and CiC models have been studied recently by Wen et al. (2020), showing the possibility to observationally test these models for various cosmologies.

The GQED (Eq. 1) can be approached as a two-parameter distribution, in terms of  $\bar{N}$  and  $b$ . However, the clustering of galaxies in terms of the GQED can be described self-consistently with no free parameters, because the clustering parameter  $b$  can be expressed also in terms of the variance of the CiC distribution (e.g., Saslaw 2000):

$$\langle(\Delta N)^2\rangle = \frac{\bar{N}}{(1-b)^2}, \quad (3)$$

or,

$$b = 1 - (\bar{N}\bar{\xi}(V) + 1)^{-1/2}, \quad (4)$$

where  $\bar{\xi}$  is the volume integral of the two-point correlation function. As can be seen from the alternative expressions for  $b$  (Eqs. 2-4), this parameter naturally depends on the cell volume (size) and is a measure of pairwise clustering and its statistical fluctuations in terms of counting cells.

The same self-consistent description can be made for the NBD model, for its corresponding aggregation parameter  $g$  (see, e.g. [Yang & Saslaw 2011](#)), where the NBD is given by:

$$f_{\text{NBD}}(N) = \frac{\Gamma\left(N + \frac{1}{g}\right)}{\Gamma\left(\frac{1}{g}\right) N!} \frac{\bar{N}^N \left(\frac{1}{g}\right)^{\frac{1}{g}}}{\left(\bar{N} + \frac{1}{g}\right)^{N + \frac{1}{g}}}, \quad (5)$$

and  $g$  is simply  $\bar{\xi}(V)$ :

$$g = \bar{\xi}(V) = \frac{\langle(\Delta N)^2\rangle - \bar{N}}{\bar{N}^2}. \quad (6)$$

It has been argued that the NBD violates the second law of thermodynamics ([Yang & Saslaw 2011](#); [Saslaw & Fang 1996](#)), even though it provides a good agreement with observations (e.g., [Hurtado-Gil et al. 2017](#)), and could possibly be identified with a model in which galaxies are preferentially aggregated where there is already an initial “seed” or cluster, but not representing an infall. Therefore, the NBD model is still a provisionally useful approximation.

We directly fit the GQED and NBD models with the respective  $(\bar{N}, b, g)$  as free parameters, where the average counting per cell  $\bar{N}$  occurs in both the GQED and the NBD models (we use the same notation, but specify either model when necessary), whereas the clustering parameters  $b$  and  $g$  refer to those appearing in the expressions for the GQED and the NBD, respectively (c.f. Eqs. 1 and 5).

The fittings were performed using the `curve_fit` module in the `scipy` library [Jones et al. \(2001\)](#). We chose the `lm` optimization method (Levenberg-Marquardt algorithm) in the case of the GQED model fitting, and the `trf` (Trust Region Reflective algorithm, with parameter bounds set to 0 and  $\infty$ ) for the case of the NBD model fitting, which has proven necessary for achieving convergence. For handling large values of  $N$  for the factorial evaluation, we used the Python module `Decimal`. The fittings were performed on CiC histograms with variable bins widths,  $dN$ , which mainly depended on the cell size. After a series of tests, the bin widths also had to be adjusted for different redshifts, because of the size and spread of the CiC population as a function of redshift. The bin widths  $dN$ , as a function of redshift and cell radius, were:

- For TNG 100-3 and TNG 100-1-Mock:  
 $dN_{\mathcal{R}'_a}(z = 0) = \{1, 10, 25, 50\}$ , and  
 $dN_{\mathcal{R}'_a}(z = 5) = \{1, 5, 10, 10\}$ .
- For TNG 300-3:  
 $dN_{\mathcal{R}_a}(z \leq 3.01) = \{1, 10, 30, 50\}$ ,  
 $dN_{\mathcal{R}_a}(z > 3.01) = \{1, 1, 1, 2\}$ ; and  
 $dN_{\mathcal{R}_b}(z \leq 3.01) = \{1, 3, 10\}$ ,  
 $dN_{\mathcal{R}_b}(z > 3.01) = \{1, 1, 1\}$ .

In the notation above, bin widths (inside brackets) are listed in the same order as the corresponding sets of cell radii (c.f. Sec. 2.2.3).

### 3 RESULTS

#### 3.1 Qualitative presentation of the CiC distributions

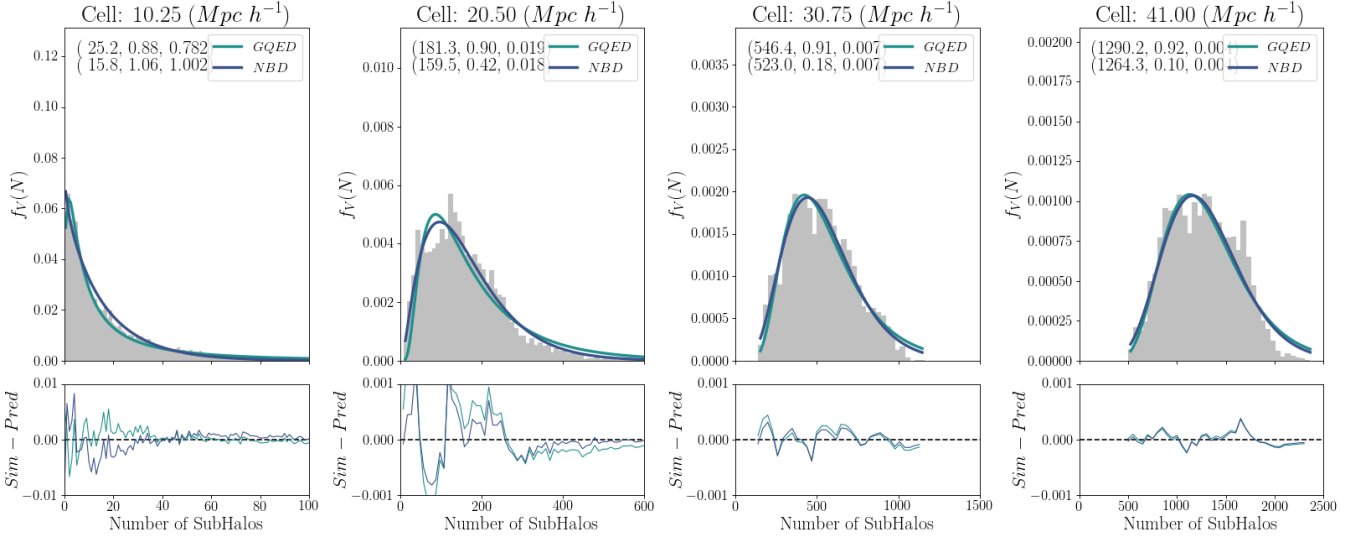
Given the large number of results (136 CiC computations, considering each run in Tab. 1, at each redshift and comoving cell size), we show in Fig. 2 a representative illustration, in which the normalized CiC histograms for the TNG-300-3 runs at redshifts  $z = 3.01$  and  $z = 0$  are presented, for the  $\mathcal{R}_a$ -set of cell radii. That figure follows the usual representation for CiC histograms in the literature (e.g. [Itoh et al. 1988, 1993](#); [Yang & Saslaw 2011](#); [Hurtado-Gil et al. 2017](#)). Note that the same scale is set for the x-axis at each comoving cell size, which allows a direct comparison of the major evolutionary effect on the CiC distribution for a given cell size. Note also that at each bin, the height of the histogram gives the value of the sampled CiC PDF, so that the integral over the range is 1.

The triplet of numbers in the legend at the top of each panel of Fig. 2 indicates the best fit values for  $(\bar{N}, b, \mathcal{B})$  for GQED (Eq. 1), and  $(\bar{N}, g, \mathcal{G})$  for NBD (Eq. 5), where  $\mathcal{B}$  and  $\mathcal{G}$  are the residual 2-norms of the GQED and NBD fits respectively. In the App. B, we present the results of the residual 2-norms for all the simulations here investigated, as a function of redshift and cell size. The individual residuals, given by the CiC histogram bin height (“Sim”) minus the best fit curve value at that bin (“Pred”), are shown in the lower panels in Fig. 2. A study of the behaviour of the best-fit parameters in terms of redshift and cell size is given in Sec. 3.2.

While the results of this project were being analyzed, a recent paper by [Wen et al. \(2020\)](#) came to our attention. These authors used the DEUS runs ([Alimi et al. 2012](#)) to study whether the CiC PDFs of halos, which were fit to several different models, could distinguish between different dark energy cosmologies. These simulations have box lengths of 648 Mpc  $h^{-1}$ ,



$$z = 0.0$$



$$z = 3.01$$

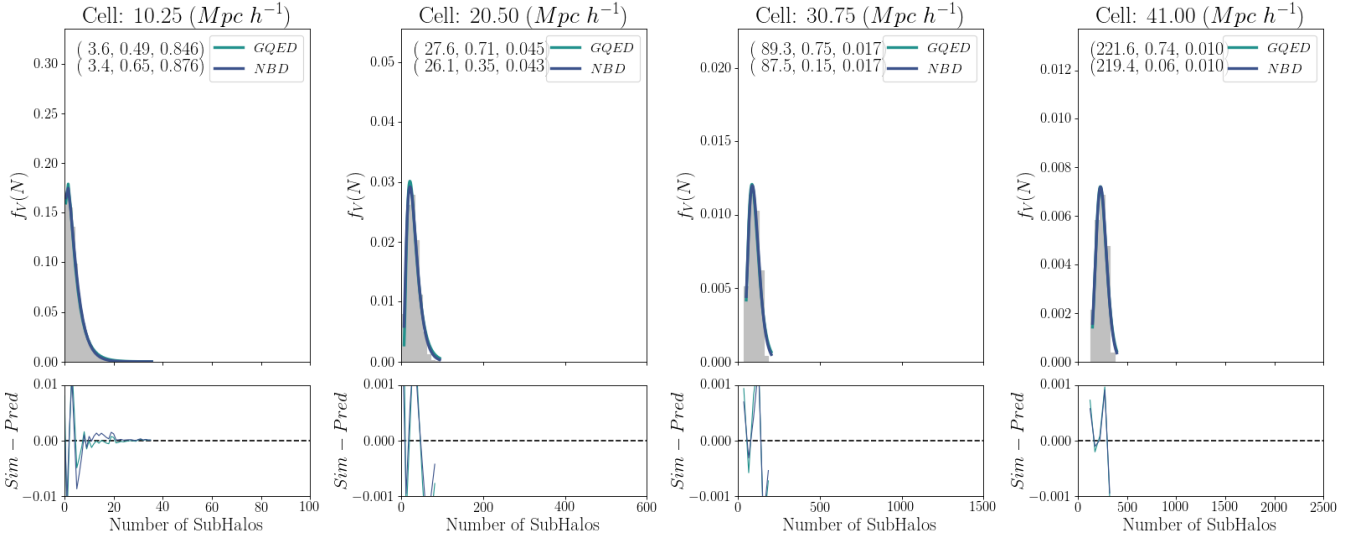


**Figure 2.** (Color online). Normalized CiC histograms for the TNG-300-3 “full” runs, for redshifts  $z = 0.0$  (top) and  $z = 3.01$  (bottom). Left to right: cell radii given by  $\mathcal{R}_a$  (c.f. Tab. 1). Light (green) line: GQED best-fit curve; dark (blue) line: NBD best-fit curve. The triplet of numbers in the legend indicates the best fit values for  $(\bar{N}, b, \mathcal{B})$  for GQED, and  $(\bar{N}, g, \mathcal{G})$  for NBD, where  $\mathcal{B}$  and  $\mathcal{G}$  are the residual 2-norms of the GQED and NBD fits respectively. The residuals are shown in the lower panels below each histogram. The histograms are normalized, such that the integral over the range equals to 1, hence the displayed values refer to the probability density function at the corresponding bin.

with  $2048^3$  DM particles, in which they used a minimum halo mass of  $M_{\text{halo}} > 2.4 \times 10^{11} M_{\odot}$  for the CiC procedure, studied as a function of scale and redshift. We follow their panel representation of CiC distributions (c.f. their Fig. 3), displaying compactly all our normalized CiC PDFs (note the log-log scale), as shown in Figs. 3 and 4 for the TNG300-3 and TNG100-3 runs, respectively. We also present the TNG-100-1-Mock results (Fig. 4, top right panel) with TNG100-3 “full” results together in the same panel for direct comparison. Finally, we present in Fig. 4, bottom right panel, a comparison between TNG300-3 and TNG100-3, for the “full” runs at  $z = 0$ .

We list some qualitative characteristics of our CiC distributions. Generally, they agree with previous numerical results in the literature, even though being purely gravitational ones (no baryonic or dissipative physics included), i.e., following the Newtonian evolution of one-component (“dark”) particles for different background cosmologies, with either unit or different

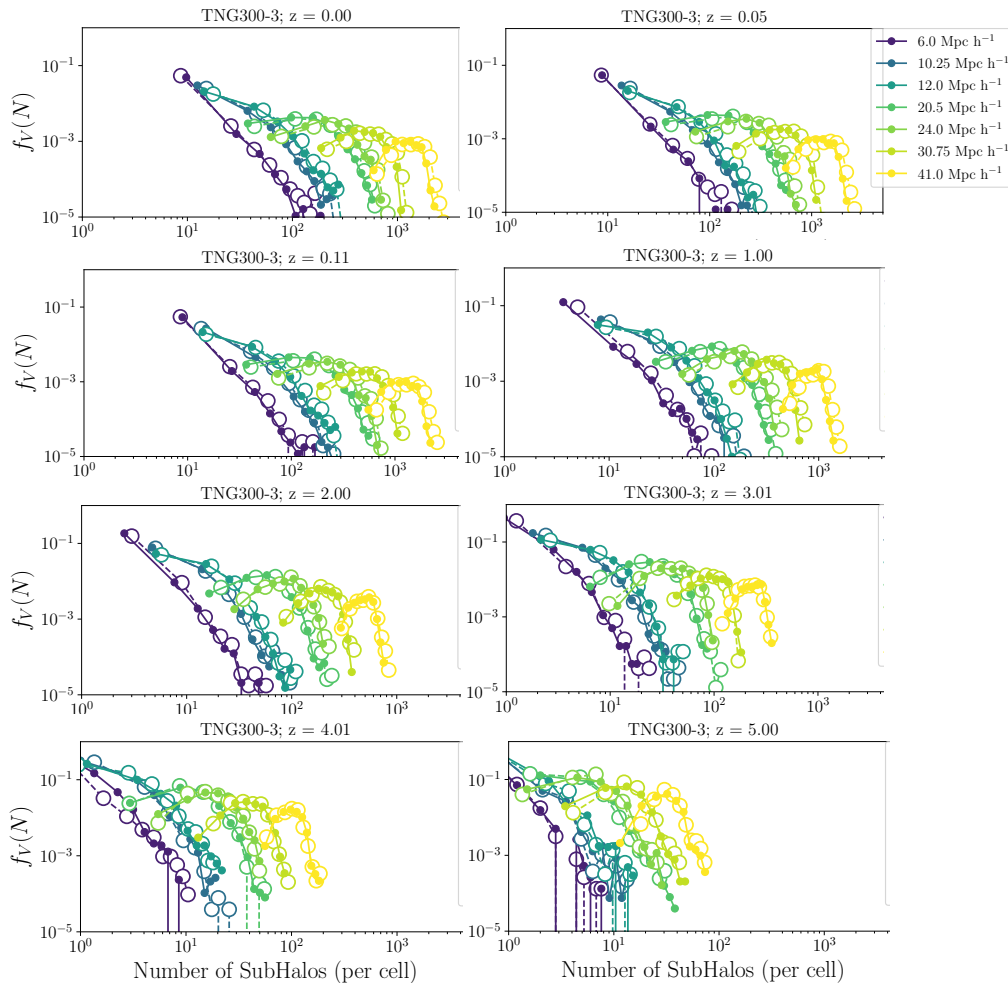


**Figure 3.** (Color online). Normalized CiC histograms (in log-log scale) for the TNG-300-3 simulations, starting from redshift  $z = 0.00$  (top, left) to  $z = 5.00$  (bottom, right), for comoving cell sizes indicated in the legend (covering both  $\mathcal{R}_a$  and  $\mathcal{R}_b$  sets, c.f. Tab. 1). Darker colors are used for smaller radii. The number of bins in this representation is fixed to  $N_{\text{bins}} = 10$ . Symbols are used instead of histogram bars: smaller (filled) circles connected with continuous lines for the “full” runs; larger (empty) circles connected with dashed lines for the corresponding “dark-only” runs.

mass ratios (e.g. Itoh et al. 1988, 1993, respectively). Our results can also be compared with those by Wen et al. (2020), which represent the latest analysis in this line of research at the time of this writing. Our results can also be compared with CiC statistics related to the GQED and NBD models applied to observational studies (e.g. Yang & Saslaw 2011; Hurtado-Gil et al. 2017). However, care must be taken to make those comparisons when considering the more quantitative behaviour of the best-fit parameters. This will be addressed with more detail in Sec. 3.2.

We list the main general or qualitative trends of our CiC results:

- *Comparison between “full” and “dark-only” simulations:* both follow remarkably similar CiC distributions, in both the TNG300-3 and TNG100-3 runs. There are, however, differences which can be finely traced by a quantitative analysis of the best-fit parameters, to be discussed in Sec. 3.2.
- *Spreading of the CiC PDF:* all CiC distributions tend to gradually spread towards  $z = 0$  as more subhalos are formed and the gravitational clustering evolves.
- *Height of the CiC PDF peak in terms of cell size:* it decreases for larger cell sizes due to spreading and normalization, even considering a larger number of samplings.
- *Height of the CiC PDF peak in terms of redshift:* it decreases for lower redshifts, as the distribution spreads into a wider range of  $N$ . Note, however, that in Wen et al. (2020) (c.f. their Fig. 2), the trend goes in opposite direction: the peak height decreases at higher redshifts, as the distribution spreads into a wider range of  $N$  for *physical* cell sizes, as explained in their paper. The reason for this difference appears to be due to a different measurement criterium for the counting cells. In Wen et al. (2020), the authors use physical cell sizes, whereas we use comoving cell sizes. In the former case, one is probing a

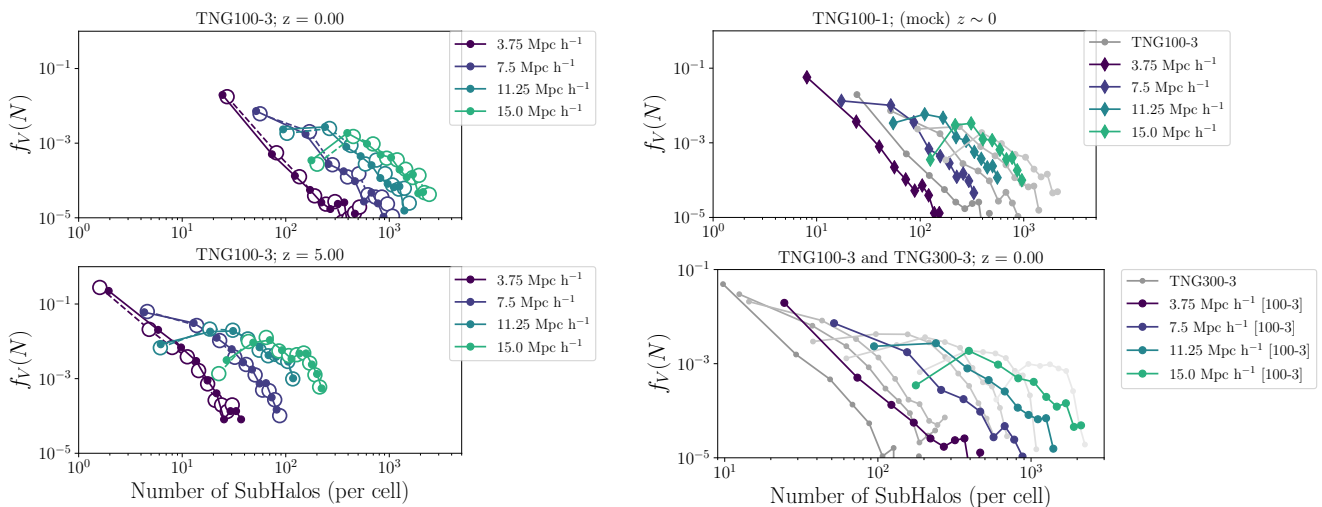


**Figure 4.** (Color online). Normalized CiC histograms (in log-log scale) for the TNG-100-3 simulations. *Left panels:* redshift  $z = 0.0$  (top) and  $z = 5.00$  (bottom). *Right panels:* in the top panel, the TNG-100-1-Mock run, with diamond symbols, whereas filled circles in grayscale represent the results for TNG-100-3 “full” at  $z = 0.0$ ; in the bottom panel, the TNG100-3 “full” distributions are compared with those of the TNG300-3 “full” runs (both at  $z = 0.0$ ).

physical volume (as defined at  $z = 0$ ), which, due to expansion, encloses a larger volume at higher redshifts, whereas we follow the same comoving volume.

- *Quality of the CiC statistics:* our statistics is necessarily poorer for higher redshifts and smaller cell sizes, as the total number of subhalos available for the comoving counting (gravitationally bound structures) is less than that at  $z = 0$  (c.f. Tab. 1, column “ $N_{\text{sh}}$ ”). In Wen et al. (2020), the CiC distribution was found to be less smooth in larger cells at higher redshifts; again we attribute this opposite effect given the physical (theirs) vs. comoving (ours) counting cell method.

- *Behaviour of the CiC for the smallest cell size:* in this case, the distribution tends to the Poisson limit, as cells may contain a very small number of subhalos, or no subhalo. This can be noticed in the qualitative form of the curve for the 10.25 [Mpc  $h^{-1}$ ] cell in Fig. 2 (at both redshifts), which also presents the lowest value of  $b$ .

- *Comparison between different simulation volumes:* we find that both simulations cover (approximately) similar  $N$  ranges in their CiC PDFs, even though the comoving cell sizes are different. E.g., for  $z = 0$ , this can be directly seen in Fig. 4 (bottom panel at right). In particular, for cells defined by the same fixed fractions of the simulation volume (i.e., the  $\mathcal{R}_a$  and  $\mathcal{R}'_a$  sets), the CiC PDFs at the high end of  $N$ , in both volumes, tend to agree at each cell size, but systematically differ for smaller  $N$  ranges.

### 3.2 Quantitative analysis of the best-fit parameters

In this section, we present the behaviour of the best-fit parameters of the GQED and NBD (c.f. Eqs. 1 and 5, respectively) as a function of redshift and comoving cell radius. The parameters are: the average number of subhalos per cell,  $\bar{N}$  (which occurs in both the GQED and the NBD), and the clustering parameters  $b$  (GQED) and  $g$  (NBD). These best-fit parameters were obtained from the CiC PDF fit to the GQED and NBD models, as explained in Sec. 2.3.

In Fig. 5, we show the best-fit average number of subhalos per cell as a function of redshift, for the TNG300-3 runs (GQED: left panel; NBD: right panel). The “full” and “dark-only” runs follow closely the same overall behaviour of this parameter. We note, for both models, a rapid evolution of  $\bar{N}$  towards higher values (above an order of magnitude from  $z = 5$  to  $z = 2$ ), with a more gradual increase thereon, up to  $z = 0$ . There is also a clear, distinctive sense in which larger cell sizes result in increasingly larger  $\bar{N}$ ’s for all the cases, which is expected. We note that the  $\bar{N}$  parameter, for the 12 Mpc  $h^{-1}$  cell, indicates an “excess” at  $z = 0$ . The results for the TNG300-3-H case are compatible with the corresponding TNG-300-3 ones at same redshift and cell sizes, also presenting a similar “excess” for the 12 Mpc  $h^{-1}$  cell.

In order to see more clearly distinctions between the “full” and “dark-only” results, we show in the bottom panels of Fig. 5 the fractional difference between these runs, relatively to the “full” runs, as a function of redshift, for the given cell sizes. Overall, both “full” and “dark-only” runs present a similar evolution of the  $\bar{N}$  parameter in the “rapidly evolving phase” at

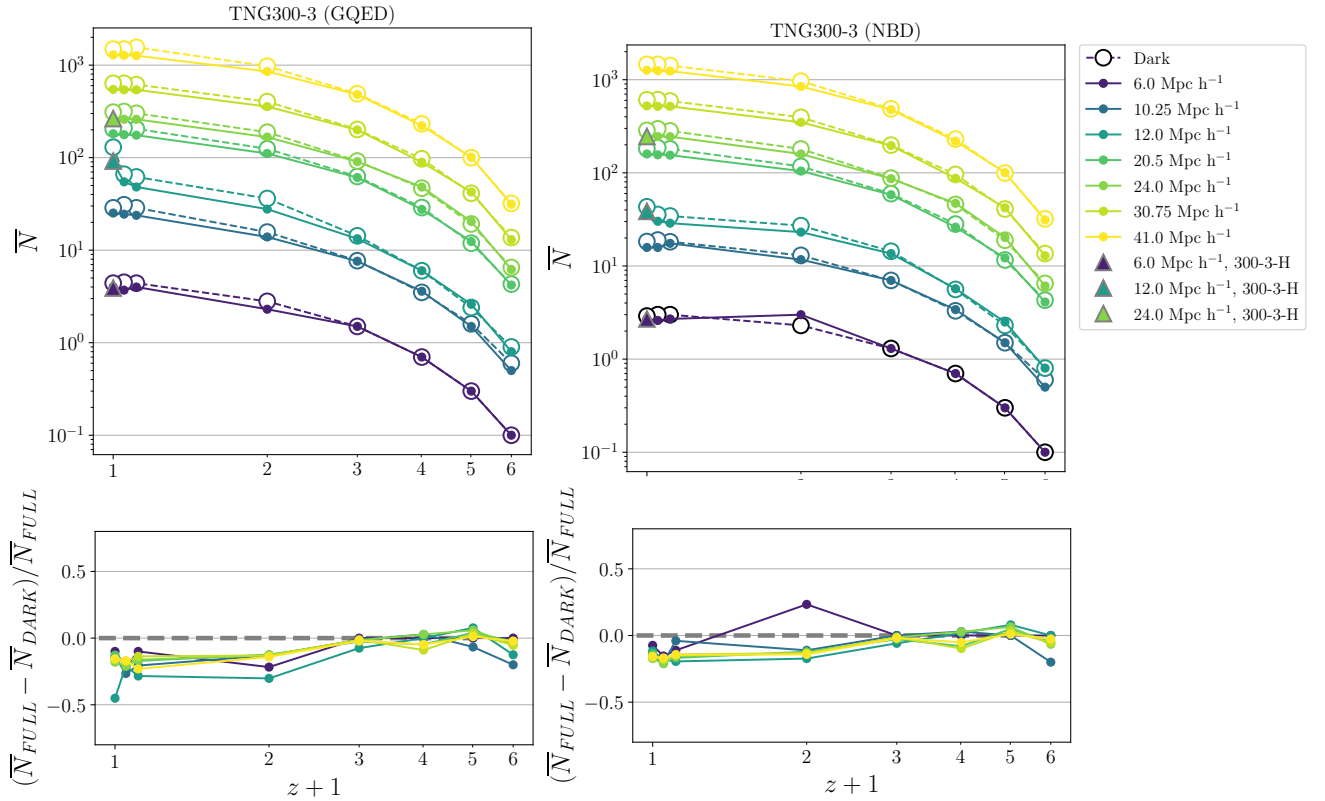


**Figure 5.** (Color online). Results for the TNG300-3 simulations, redshifts  $z = \{0.00, 0.05, 0.11, 1.00, 2.00, 3.01, 4.01, 5.00\}$ , for various comoving cell radius (darker colors for smaller radii, see legend). Filled circles connected with continuous lines refer to the “full” simulation runs; larger, empty circles connected with dashed lines refer to the respective “dark-only” simulation runs. The TNG300-3-H (“full”) runs are represented by triangles at  $z = 0$ . *Top panels:* behavior of the average number of subhalos per cell,  $\bar{N}$ , as a function of  $z$ , obtained from the CiC PDF fit to the GQED (left panel) and NBD (right panel) models. *Bottom panels:* fractional difference between “full” and “dark-only” results, relatively to the “full” runs (GQED: left panel; NBD: right panel).

$2 \lesssim z \lesssim 5$ , for all cell sizes in this redshift range, but at lower redshifts, the  $\bar{N}$  parameter tends to be systematically higher for the “dark-only” runs. This effect is small ( $\lesssim 5\%$ ) but clearer in the GQED case.

Next, still for the TNG300-3 runs, we present in Fig. 6 the results for the clustering parameters  $b$  (GQED; left panel) and  $g$  (NBD; right panel), in terms of redshift and cell size, in the same format as in the previous figure (Fig. 5). For the GQED, we see a clear trend, for both “full” and “dark-only” runs and for all cell sizes, showing smaller values of  $b$  at higher redshifts to greater values of  $b$  at lower redshifts. Smaller cells (at fixed redshift) tend to show smaller values of  $b$ . Note that, again, the behaviour of  $b$  for the cell size  $12 \text{ Mpc h}^{-1}$  presents a deviation from this overall trend, signaling larger values of  $b$  for  $z \lesssim 3$  as compared to all other cells.

For the NBD,  $g$  values are generally larger for smaller cell sizes, with the results for the  $12 \text{ Mpc h}^{-1}$  cell also presenting some deviation from the overall trend for  $z \lesssim 3$ , but the effect is smaller. Note that, from Eq. 6, the behaviour of  $g$  is consistent with that of the correlation function (higher values for smaller cell sizes; e.g., Springel et al. 2018, their Fig. 1). However, for smaller cell sizes, we observe an inversed trend towards higher values of  $g$  at  $z > 3$  as compared to those at smaller redshifts, which are not expected from the evolution of the two-point correlation function.

The bottom panels of Fig. 6 show the fractional difference between “full” and “dark-only”  $b$  (GQED) and  $g$  (NBD) results, relatively to the “full” runs, as a function of redshift, for the given cell sizes. Overall, both “full” and “dark-only” runs present a remarkably similar evolution of their respective clustering parameters at redshifts  $z \lesssim 2$ , with greater values of  $b$  and  $g$ , for the “full” runs and for larger cell sizes at  $z = 5$ .

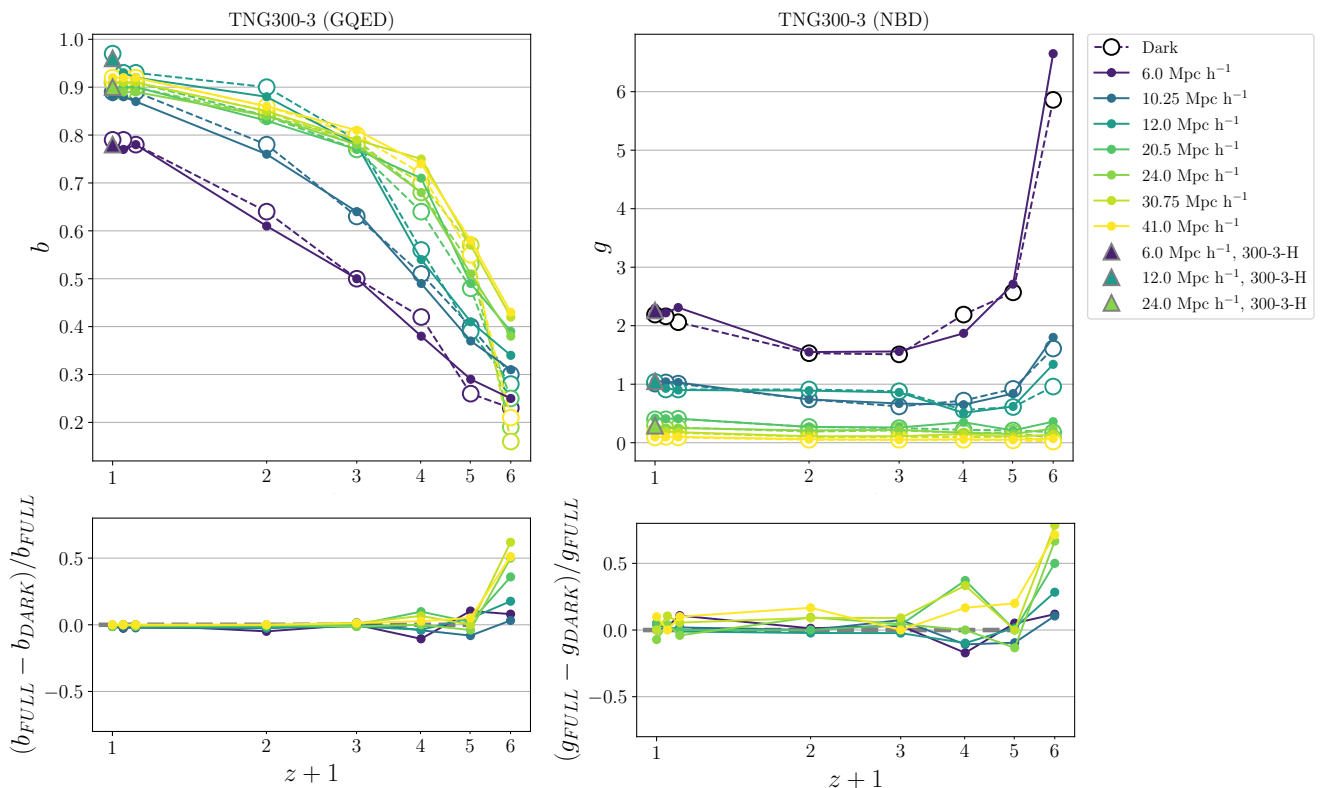


**Figure 6.** (Color online). Results for the TNG300-3 simulations, redshifts  $z = \{0.00, 0.05, 0.11, 1.00, 2.00, 3.01, 4.01, 5.00\}$ . *Top panels:* behavior of the clustering parameter as a function of  $z$ , obtained from the CiC PDF fit to the GQED ( $b$  parameter; left panel) and NBD ( $g$  parameter, right panel) models, for various comoving cell radius, as indicated in the legend. *Bottom panels:* fractional difference between “full” and “dark-only” results, relatively to the “full” runs (GQED: left panel; NBD: right panel). Symbols are the same as in the previous figure.

In Fig. 7 we present the best-fit parameter results for the TNG100-3. For this dataset, we have only analyzed the  $z = \{0.00, 5.00\}$  runs, which we connect with straight lines (only as coarse references for the evolution of the parameters). For direct comparison, we include in this figure the TNG300-3 “full” results (c.f. Figs. 5 and 6), but here are shown in the “background” of the panels in a lighter grayscale map.

We note that the TNG100-3 “full” runs at  $z = 5$  show slightly higher values of  $\bar{N}$ ,  $b$  and  $g$  than the “dark-only” runs, but this tendency is inverted at  $z = 0$ . The best-fit parameters follow the same overall trends in terms of comoving cell size as in the TNG300-3 runs, based on the  $z = 0$  and  $z = 5$  values. The main differences are the following. For the  $\bar{N}$  parameter, in both GQED and NBD, the TNG100-3 values at  $z = 5$  are higher than those of the TNG300-3 runs, but the increase of this parameter towards the values at  $z = 0$  are less than one order of magnitude, that is, a lower relative increase than in the TNG300-3 runs. An even more significant trend is found for the  $b$  parameter, with higher values at  $z = 5$  as compared to the TNG300-3 runs, but converging to those of the TNG300-3 runs at  $z = 0$ .

### 3.3 Comparison of the best-fit parameters with observations

We compare our results with those obtained by Yang & Saslaw (2011) (hereon [YS11]) and Hurtado-Gil et al. (2017) (hereon [HG17]). In [YS11], the galaxy catalog is a flux-limited ( $r < 17.6$ ) subsample taken from Sloan Digital Sky Survey (SDSS) (SDSS Abazajian et al. 2009, DR7), with additional absolute magnitude cuts, resulting in 3 subsamples within two redshift ranges, namely:  $1a(r)$ :  $0.04 \leq z \leq 0.12$ ,  $M_r < -20.2$ ;  $1b(r)$ :  $0.04 \leq z \leq 0.12$ ,  $M_r < -21.5$ ;  $2b(r)$ :  $0.12 \leq z \leq 0.20$ ,  $M_r < -21.5$ .

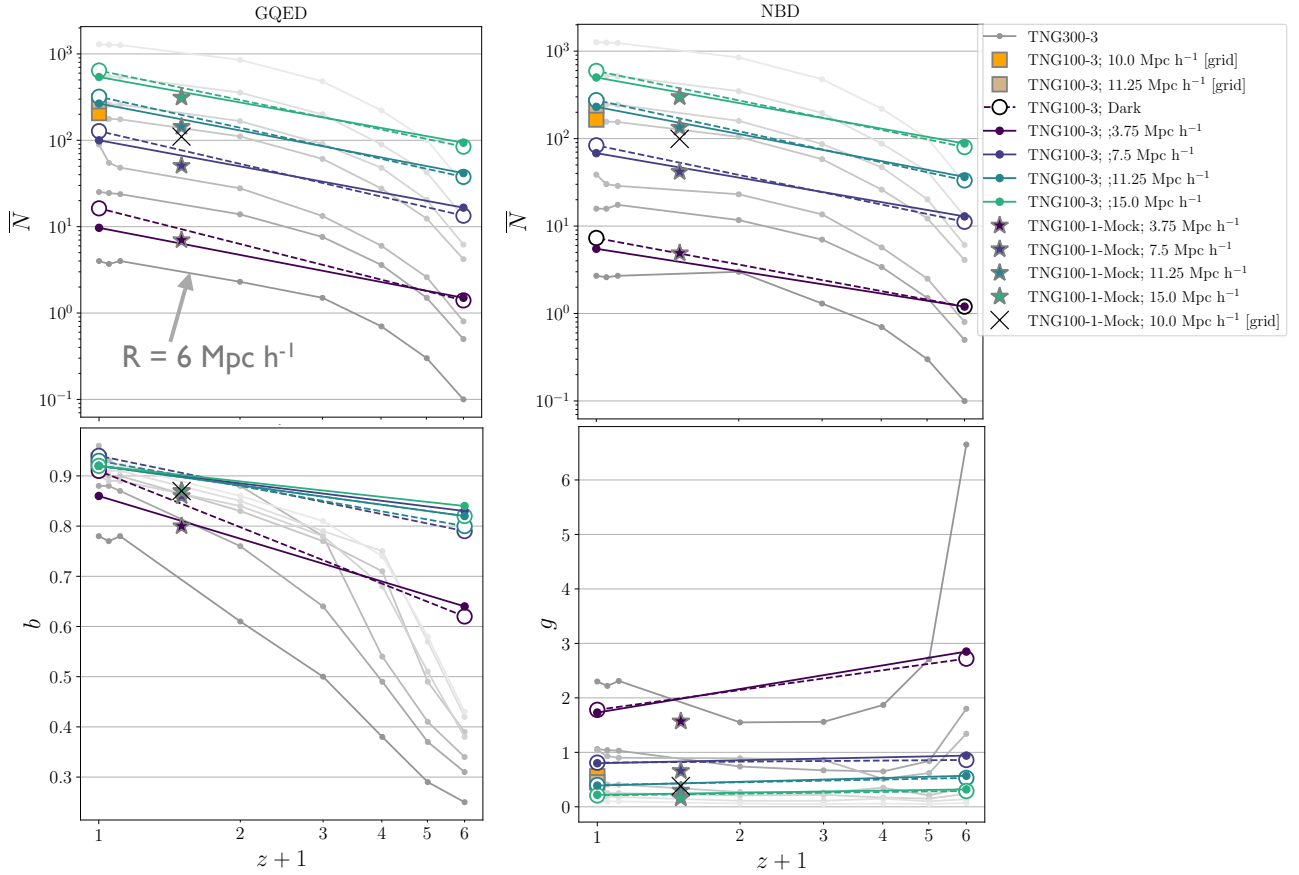


**Figure 7.** (Color online). Behaviour of the best-fit parameters for the TNG100-3 runs, for redshifts  $z = \{0.00, 5.00\}$ , which we represent by filled circles connected with continuous lines for the “full” runs, and larger, empty circles connected with dashed lines for the “dark-only” runs. Results from the TNG300-3 “full” runs are also shown with smaller circles connected with thin lines, with greyscale tones such that the darker tones represent smaller cell sizes (results for the comoving cell radius of  $R = 6 \text{ Mpc h}^{-1}$  are indicated for reference; see previous figures for more details on the TNG300-3 results). In addition, we also show the results for the TNG100-3 runs using the “Grid”-method (square symbols), as well as the results for the TNG100-1-Mock runs (star symbols), including one obtained with the “Grid”-method (cross symbol). *Top panels:* behaviour of the average number of subhalos per cell,  $\bar{N}$ , as a function of redshift, obtained from the CiC PDF fit to the GQED (left) and NBD (right) models. *Bottom panels:* behavior of the best-fit clustering parameters, as a function of redshift:  $b$  parameter (GQED, left); and  $g$  parameter (NBD, right).

The lower cut at  $z \leq 0.04$  excludes the Coma and Virgo clusters; the subsample follows the Hubble flow. On the other hand, the higher redshift range includes the SDSS “great wall”, allowing a comparison of potential differences between both ranges. In [HG17], the data was also based on the DR7, with galaxy catalog provided by The New York University - Value Added Galaxy Catalog (Blanton et al. 2005). They also used the LasDamas simulation catalog (McBride et al. 2011) to estimate the uncertainties in the resulting CiC distribution. Their selected samples are given by two populations: *Pop 1*:  $0.050 \leq z \leq 0.106$ ,  $M_r < -20.0$ ; *Pop 2*:  $0.075 \leq z \leq 0.165$ ,  $M_r < -21.0$ ; which are placed roughly within samples 1a(r) and 2b(r) from [YS11], respectively.

Before presenting our results, we point out that in [YS11] the parameters  $\bar{N}$ ,  $b$  and  $g$  were not obtained from fittings to the GQED and NBD models, but rather directly from the CiC distributions, wherein one obtains by the mean ( $\bar{N}$ ) and variance ( $\langle (\Delta \bar{N})^2 \rangle$ ) of the number of galaxies per cell and relate them to expressions involving  $b$  and  $g$  for the GQED and NBD models (Eqs. 3 and 6, respectively). Note also that, for this reason, in [YS11] the  $\bar{N}$  values are the same in both GQED and NBD cases. In [HG17], the  $\chi^2$  estimates for the best-fit parameters are provided, but we will not present them in our figures due to difficulties related to correlations between cells, which would be complicated to address consistently across different datasets (c.f. App. B).

In Fig. 8, we present the behaviour of the best-fit parameters  $\bar{N}$ ,  $b$  and  $g$  for the TNG300-3 runs, as a function of comoving

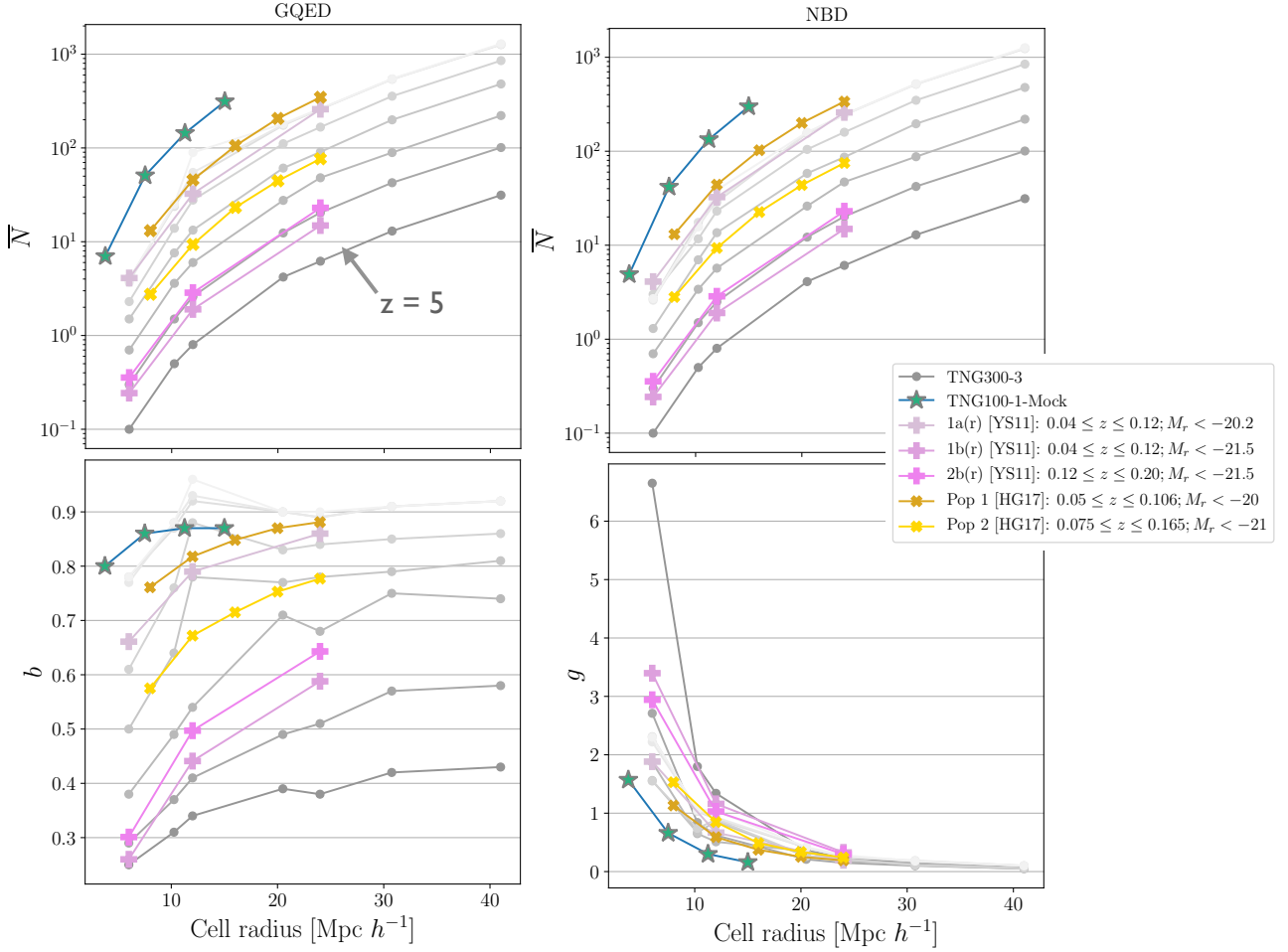


**Figure 8.** (Color online). Behaviour of the best-fit parameters for the TNG300-3 runs as a function of comoving cell size; full circles connected with thin lines are shown with greyscale tones such that the darker tones represent greater redshifts ( $z = 5$  results are indicated for reference). Also shown are the TNG100-1-Mock results, as well as those for the corresponding best-fit values for the data in [YS11], in terms of the 1a(r), 1b(r) and 2b(r) samples, are indicated. Also shown are results for the data in [HG17], for the population 1 and 2 samples. Redshift and  $M_r$  magnitude ranges for those data are indicated in the legend. *Top panels:* behaviour of the average number of subhalos per cell,  $\bar{N}$ , as a function of comoving cell size, obtained from the CiC PDF fit to the GQED (left) and NBD (right) models. *Bottom panels:* behavior of the best-fit clustering parameters, as a function of comoving cell size:  $b$  parameter (GQED, left); and  $g$  parameter (NBD, right).

cell size, for all redshifts analyzed (darker greyscale tones indicate greater redshifts, with the  $z = 5$  results indicated for reference). Also shown are the TNG100-1-Mock results, and the results from [YS11] and [HG17]. We identify the following characteristics:

- *Behaviour of  $\bar{N}$  (general trends):* all samples (observational and simulated) follow a remarkably similar behaviours in terms of cell size, for both GQED and NBD models, only differing in terms of relative amplitudes in  $\bar{N}$ . Generally,  $\bar{N}$  values grow for larger cell sizes (which is expected) and are also systematically larger for smaller redshifts (for any given cell size). The TNG100-1-Mock runs have the highest values in  $\bar{N}$  (for any given cell size).
- *Behaviour of  $\bar{N}$  (magnitude cutoffs):* One interesting inversion to the previously mentioned trend, however, is seen between the 1b(r) and 2b(r) samples, which are at different redshifts ranges but at same magnitude cutoff: the lower redshift sample, 1b(r) shows a lower amplitude in the  $\bar{N}$  values as compared to the higher redshift one, 2b(r). Note that this inversion of the overall trend (higher  $\bar{N}$  for lower redshifts) occurs despite the presence of the SDSS “great wall” in the 1b(r) sample. Also, for the same redshift range, the fainter sample, 1a(r), show higher values of  $\bar{N}$  than the brighter, 1b(r) sample. These points were already discussed in detail in [YS11].
- *Behaviour of  $\bar{N}$  (comparison between observations and simulations):* except for the 1a(r) and Pop 1 samples, which are

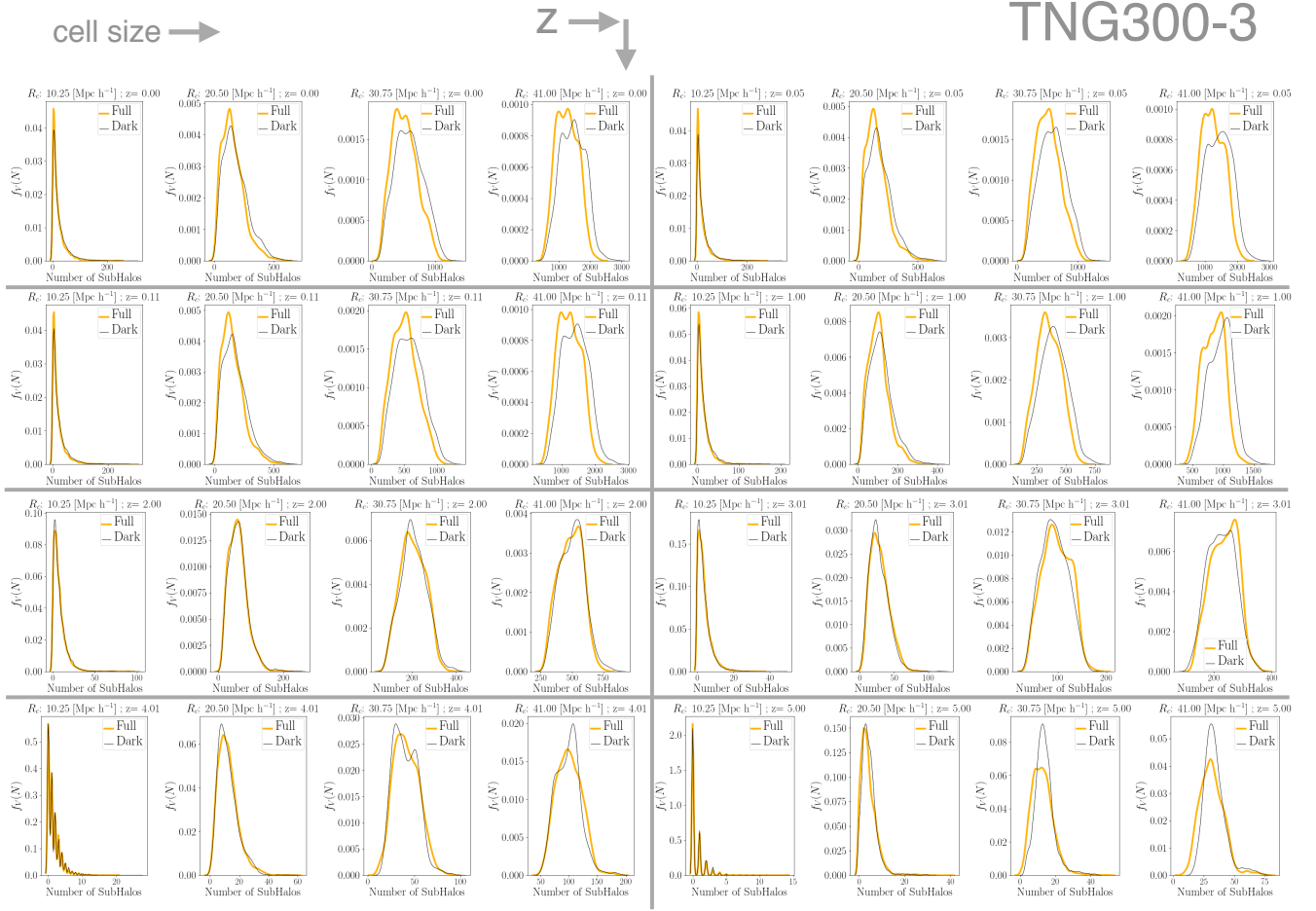


**Figure 9.** (Color online). TNG-300-3 simulations: kernel density estimate plots for the CiC PDF  $f_V(N)$ . In this 8-slot grid (one for each  $z$ ), each slot includes 4 panels, in which comoving cell sizes increase as indicated. That is, redshifts increase from the top-left slot, to the top-right, bottom-left, bottom-right, etc:  $z = \{0.00, 0.05, 0.11, 1.00, 2.00, 3.01, 4.01, 5.00\}$ . Cell radii shown for the  $\mathcal{R}_a$  set (c.f. Tab. 1). “Full” simulations: light curves; “dark-only” simulations: black curves. The horizontal scale is not the same for all panels (it increases towards higher values for larger comoving cell sizes and for lower redshifts).

fainter samples at the lower redshift range, all other (brighter) samples have lower  $\bar{N}$  values than those indicated by the TNG300-3 runs at similar redshifts, which can be generally understood as a selection effect given by the magnitude cutoffs.

- *Behaviour of  $b$* : all samples (observational and simulated) follow a similar behaviour in terms of cell size, with higher values of  $b$  for larger cell sizes, again only differing in terms of relative amplitudes in  $b$ . However, these trends are more heterogeneous across the samples and simulation runs than those found in  $\bar{N}$ . The same trend as in  $\bar{N}$  in terms of redshift is also found here: higher  $b$  values for lower redshifts. The observational samples follow the same trends in  $b$  as those in  $\bar{N}$  mentioned above, differing, though, in terms of the relative amplitudes of these trends. We point out the clear excess of  $b$  values in the 12 Mpc  $h^{-1}$  cell (for lower redshifts), which was also mentioned previously, as an “excess” in  $\bar{N}$  for  $z \sim 0$ .

- *Behaviour of  $g$* : again, all samples (observational and simulated) follow a similar behaviour in terms of cell size, with higher values of  $g$  for smaller cell sizes, only differing in terms of relative amplitudes in  $g$ . Higher values of  $g$  are found for higher redshifts, but this trend not significant for greater cell sizes.

### 3.4 Kernel density estimates

In this section, we briefly analyze the behaviour of the CiC distributions in terms of the normalized CiC kernel density estimates (KDE; note that the integral over the counting range also equals to 1). These estimates were obtained through the `sns.distplot` module (Waskom et al. 2016), in Python, with default parameters. Note that, for the figures in this section,



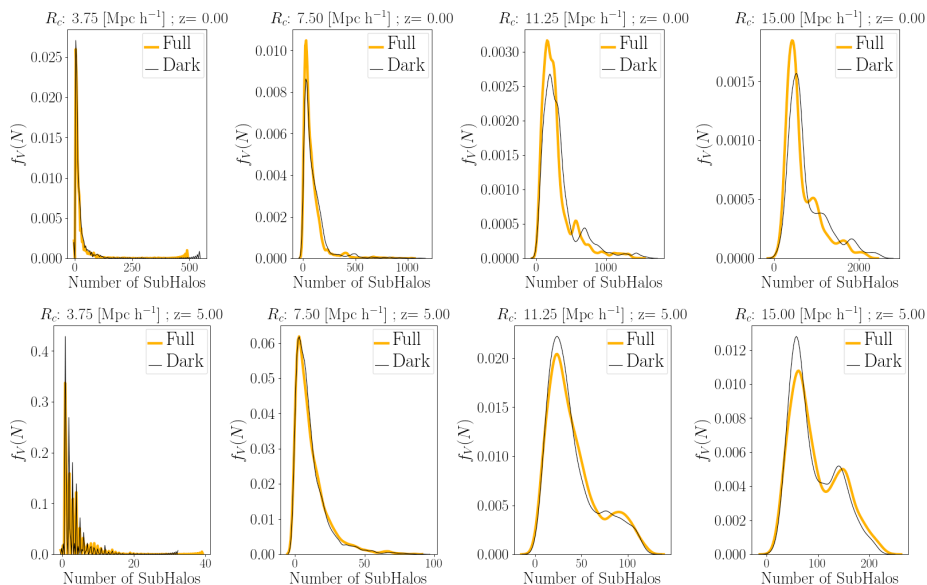


**Figure 10.** (Color online). TNG-100-3 simulations: kernel density estimate plots for the distribution  $f_N(N)$ . Top: redshift  $z = 0.00$ ; bottom:  $z = 5.00$ . Cell radii shown for the  $\mathcal{R}_a$  set (c.f. Tab. 1). “Full” simulations: light curves; “dark-only” simulations: black curves. The horizontal scale is not the same for all panels.

the horizontal scale (number of subhalos per cell) is not the same for all panels: it increases towards higher values for larger comoving cell sizes and for lower redshifts.

In Fig. 9 we present the KDE results for the TNG-300-3 runs. Both “full” and “dark-only” runs show similar distributions overall (for the smallest cell size at high redshifts, the KDE fluctuates as the kernel approaches the individual cell count, creating an artifact). We find that the KDE have Poisson-like forms for smallest cell size for all redshifts, but there are deviations for larger cell sizes and lower redshifts, favouring higher cell counts for the “dark-only” runs (the KDE curves are preferentially shifted to the right of the “full” runs). This is compatible with the results in Fig. 5, as discussed previously.

In Fig. 10 we present the KDE results for the TNG-100-3 runs. The same characteristics as those in the TNG300-3 runs are found for the smaller cell sizes. For the larger cell sizes, the KDE shows a more distinct elongation towards higher  $N$ , with a secondary peak at  $z = 5$  which evolves towards a “fluctuating”, high  $N$  “tail” at  $z = 0$ , with the “dark-only” KDE curves also shifting to the right of the “full” runs at that redshift, compatible with the results discussed in the previous section.

In summary, the “dark-only” runs tend to produce an increasingly distinctive evolution in the CiC PDF as  $z \rightarrow 0$  (for larger cells), filling the high  $N$  tail slightly more efficiently than their “full” counterparts.

#### 4 SUMMARY AND CONCLUSIONS

We investigated the properties of the Counts-in-Cells subhalo distributions in terms of the GQED and NBD models in the Illustris-TNG simulations, searching for potential differences between the “full” and “dark-only” runs. Our focus was not on selecting the best model between GQED and NBD, but to obtain general trends for the cases in which these models showed reasonably good approximations to the CiC distributions. Given that the results showed a good agreement overall, except for the smallest cell sizes, we were able to obtain some quantifiable indications of how the CiC distributions are affected in the presence of baryonic physics.

We summarize our main results as follows.

- Both the “full” and “dark-only” runs (TNG100-3 and TNG300-3) follow, overall, similar CiC PDFs (c.f. Figs. 3 and left panels of Fig. 4). All CiC distributions gradually spread towards  $z = 0$ , as more subhalos are formed in the comoving box and the gravitational clustering evolves. Both TNG100-3 and TNG300-3 cover similar  $N$  ranges of CiC distributions, despite their different volume boxes.
- The behaviour of the best-fit parameters  $\bar{N}$ ,  $b$  and  $g$  follow trends consistent with previous literature, as a function of redshift and cell size (for the values probed in the present work; c.f. Figs. 5, 6, 7).

- Despite the overall similarity of the CiC distributions, there are measurable differences leading to specific trends which might be relevant for the understanding of bias. For example, from the bottom panels of Fig. 6, at higher redshifts ( $z > 2$ ), “full” runs present higher clustering parameters relative to “dark-only” counterparts at every cell size, with lower  $\bar{N}$  values at  $z = 5$  (bottom panels of Fig. 5). The clustering parameters for the “full” runs becomes similar to the “dark-only” runs at lower redshifts, but then  $\bar{N}$  tends to become smaller relatively to the “dark-only” runs, specially in the GQED results. This could be an indication that subhalos in the “full” runs are merging inside common dark matter halos more efficiently than in the “dark-only” runs.

- Clustering ( $b$ ) tends to increase towards lower redshifts and to converge to similar values at  $z = 0$  (Figs. 6 and 7), with higher values for larger comoving cell sizes (c.f. Fig. 8), compatible with the scale dependence of this parameter (c.f. Saslaw & Crane 1991; Sheth & Saslaw 1996). The  $g$  parameter presents higher values for smaller cell sizes, compatible with the expected behaviour of the two-point correlation function (c.f. Springel et al. 2018). However, for  $z > 3$  and small cell sizes (Fig. 6), there is an increase in  $g$ , which is  $\sim 5\%$  more pronounced relatively to the “dark-only” runs. More investigation is necessary in order to address the origin of this result.

- For the TNG300-3 (both “full” and “dark-only”) runs, for the 12 Mpc  $h^{-1}$  cell, we found an “excess” in the parameters  $\bar{N}$  (at  $z = 0$ ) and in  $b$  ( $z \lesssim 3$ ), as compared to the relative behaviour of these parameters in other cells. This could be an indication that, at this cell size, relaxation occurred rapidly ( $z \lesssim 3$ ) among several near neighbors cells at that scale, as compared to larger scales.

- All CiC distributions converge to similar  $b$  values ( $b \sim 0.9 \pm 0.05$ ) at  $z = 0$ , in both the TNG100-3 and TNG300-3 (“full” and “dark-only”) runs, except for the smallest cell size. The results for the smallest cell sizes could be affected by a poor statistics, as discussed in the Apps. A and B, and should be interpreted with care. The relative “convergence” of  $b$  values, with small dispersion, indicates that there was time for relaxation to proceed at the scales analyzed.

- Comparing our results with previous numerical, observational and “mock” catalogs, we found similar scaling and evolutionary trends in all samples, up to factors in the amplitude of parameter values, possibly regulated by different magnitude cutoffs in the observational samples.

- The TNG100-1-Mock results show the highest values in  $\bar{N}$  and in clustering parameters ( $b$  and  $g$ ) for all cell sizes analyzed. The reason for this effect is unclear, but probably results from the selection of the catalog. From Tab. 1, the total number of subhalos available for the CiC procedure in the TNG100-1 at  $z \sim 0$  is  $N_{\text{sh}} = 4371211$ , much larger than the number of “mock” galaxies in the catalog used for the counting, 11427. Hence, the sample used does not seem to trace the underlying CiC distribution, at least when compared with TNG100-3 and TNG300-3 results (c.f. Figs. 4 and 8).

- Normalized CiC kernel density estimates indicate qualitative agreement with the above results obtained from GQED and NBD model fittings, with variations between the “full” and “dark-only” runs, specially more visible in the larger cell sizes. The TNG100-3 runs shows a “bimodality” in the large  $N$  tail at  $z = 5$  (in larger cell sizes), which spreads into a fluctuating, longer high  $N$  tail at  $z = 0$ .

From the analysis of the residues (App. B), we have evidence that the quasi-equilibrium evolution is a good approximation for the large scale clustering in the Illustris-TNG simulations, for  $z \lesssim 5$ . However, for the smallest cell sizes (6 Mpc  $h^{-1}$  for the TNG300-3 and 3.75 Mpc  $h^{-1}$  for the TNG100-3) we found large residues, giving poorer fits. The residues also tend to increase somewhat for higher redshifts in the TNG300-3 runs (for cell sizes 10.25 and 12 Mpc  $h^{-1}$ ). In App. A, we mention the limitation of our statistics in terms of cell sizes, at each redshift, which is more problematic for the smallest cells. In principle, the larger residues found in the smallest cells would indicate less compatibility with GQED, in the sense that the quasi-equilibrium state would not be valid at such scales (i.e., approaching the nonlinear regime). However, given the limitation of our statistics at those scales, further analysis is necessary, with a larger number of counting cells (at least at the order of the number of subhalos).

Although our aim was not to identify the best model (between the GQED and the NBD) for the distribution function  $f_V(N)$ , but to address potential differences between the “full” and “dark-only” runs, by the use of independent models, we found that both the GQED and the NBD fit reasonably well the CiC distributions, in agreement with Yang & Saslaw (2011). Note that the NBD model has been shown to be unphysical (Saslaw & Fang 1996), even though it does provide a good fit to the observed  $f_V(N)$  (e.g. Hurtado-Gil et al. 2017). It is interesting to point out that, even if unphysical, the NBD also provides a reasonable fit for cosmological simulations with the inclusion of baryonic physics, such as the Illustris-TNG simulations. Hence, our results suggest the overall validity of those models for describing the large-scale statistics of extended, multi-component gravitational systems of different masses and subject to complex baryonic physics.

The theory leading to the GQED, in its original form (as considered here), assumes that all galaxies (here, subhalos) have the same mass. However, the Illustris-TNG subhalos have different masses as they are obviously multicomponent, extended particle systems. Yet, it is clear from our results that such a gravithermodynamical theory does provide, to “first order”, a description of the large-scale gravitational clustering, even in the presence of additional complexity. Indeed, Itoh et al. (1993) investigated cosmological simulations using a spectrum of particle masses (each representing a galaxy), in which differences in the clustering behaviour, relatively to single-component simulations, were observed. These earlier simulations indicated that

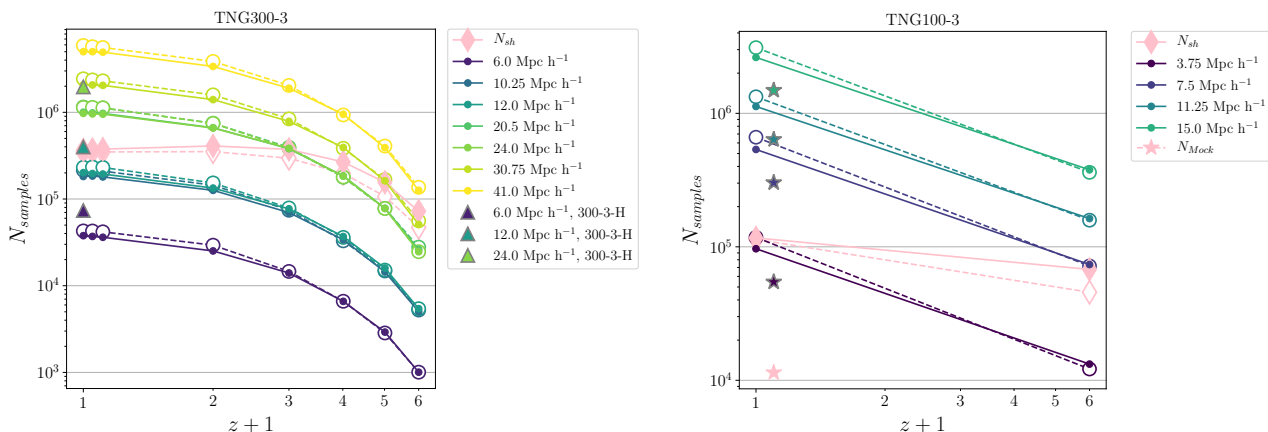


**Figure A1.** (Color online). Number of cell samplings for the TNG-300-3 (left) and TNG-100 (right) runs (both “full” and “dark-only” runs), as a function of redshift and cell size. Also shown (diamond symbol) are the actual number of subhalos in the respective simulations at each redshift.

an initial mass spectrum does affect clustering in cosmological contexts, and the GQED would still provide a good description of the CiC distribution, except in certain conditions, particularly related to the size of sampling volumes relatively to the simulation box and the dominance of satellite systems. Our results also indicate the broad validity of the GQED for extended (multi-component) subhalos of different masses. The dependence of subhalo mass on the CiC distribution in the context of the GQED is left for a future work.

Finally, our results indicate that the overall properties of non-linear gravitational clustering in the presence of baryonic physics can be reasonably described by the basic principles of a gravithermodynamical, quasi-equilibrium evolution theory, such as GQED. Fitting the CiC distributions to the GQED indicates that both “full” and “dark-only” simulations do follow such principles, but with quantifiable differences arising from multicomponent dynamics and complex small scale physics. Additional theoretical work is necessary to refine such a theory in order to predict the differences such as the ones described qualitatively here. The development of theoretical predictions for the nature and evolution of bias from gravithermodynamical principles, allied with increasingly refined numerical simulations, points to a valuable line of research.

## ACKNOWLEDGEMENTS

CCD thanks dr. Hugo V. Capelato for his encouragement for the development of this project.

## APPENDIX A: ANALYSIS OF THE CELL SAMPLING

In this section, we evaluate the relative impact of the choice of the number of comoving cells in our CiC procedure. We present an analysis of the dependence of the number of cell samples in terms of redshift and cell sizes. It has been noted (Yang & Saslaw 2011; Hurtado-Gil et al. 2017) that a CiC statistics with a relative good quality can be generally obtained by taking the number of counting cells of the order of the number of (observed or simulated) galaxies. We study the effect of doubling (from 9500 to 19000) the number of cells for the “full” TNG300-3 run at  $z = 0$ , using the “Rand”-method [IIS88], as discussed in Sec. 2.2.2; this case is denoted by “TNG-300-3-H” in Tab 1.

In that method, we have overlapping cells, so each cell will contain a certain number of subhalos, in which part of them will be counted again in some overlapping cells. Let  $N_{\text{samples}}$  denote the total number of subhalos counted in total, allowing for such repeated counts. In Fig. A1, we present  $N_{\text{samples}}$  as a function of redshift and cell size for the TNG-300-3 and TNG-100 (both “full” and “dark-only”) runs, as well as the TNG-300-3-H results. Also shown is the actual number of subhalos,  $N_{\text{sh}}$  (which met the criteria established in Sec. 2.2.3).

Considering the available statistics from the overlapping cells resulting in data with size of the order of  $N_{\text{samples}}$ , we see in Fig. A1 that such criteria is achieved for most cases, except the smallest cell sizes, specially at high redshifts, where we have mentioned previously that the CiC statistics is indeed poorer (see also App. B on residues). Considering the TNG-300-3-H case, the doubling of the number of counting cells leads only to a linear increase on the resulting  $N_{\text{samples}}$  (at least for  $z = 0$ ). We conclude that the CiC statistics for the smallest cell size would require at least an order of magnitude increase in the number of counting cells in order to reach the criteria above, so our results for the smallest cell size in both TNG100-3 and TNG300-3 runs should be considered less certain.

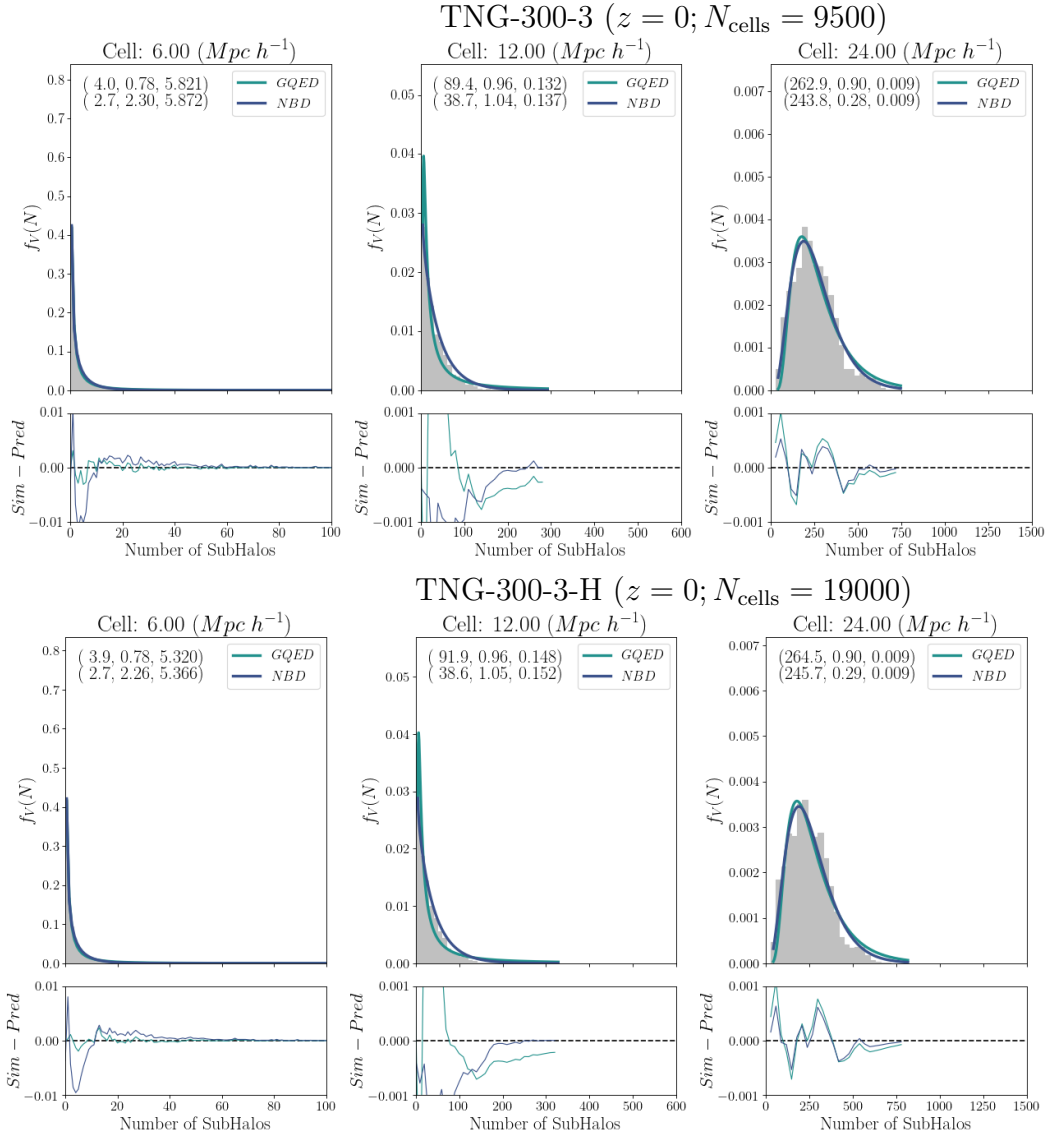


**Figure A2.** (Color online). Histograms for the TNG-300-3 (top) and TNG-300-H simulations (down) at  $z = 0$ .

In Fig. A2 we present a comparison of the histograms for the TNG-300-3 and TNG-300-H simulations at  $z = 0$ . The results are quite similar, with very close best-fit parameters. Note that the excess in  $\bar{N}$  and  $b$  at 12 [Mpc  $h^{-1}$ ] cell, mentioned in the main text, are also seen in the TNG-300-3-H case.

Wen et al. (2020) used a similar “grid”-type method as in [Lei19] (c.f. Sec. 2.2.1), with the centers of a regular  $512^3$  grid as the centers of the spherical (overlapping) counting cells. Considering their larger number of cells than in our work, they obtain smoother  $f_V(N)$ ’s. Even though they use a higher value for the minimum mass ( $M_{\text{halo}} > 2.4 \times 10^{11} M_{\odot}$ ) than in our work ( $2.5 \times 10^8 [M_{\odot} h^{-1}]$ ,  $h = 0.6774$ ; c.f. Sec. 2.2.3), this resulted in their case a friends-of-friends halo count of  $N_{\text{halo}} = 3045305$  (with a minimum of 100 particles per halo), which is about an order of magnitude greater than those in our analysis of the TNG simulations. We refer the reader to their App. A for a rigorous analysis of CiC resolution estimates.

## APPENDIX B: ANALYSIS OF RESIDUES

In this section we present a brief analysis of the residues in the CiC fits to the GQED and NBD models for the TNG100-3 and TNG300-3 runs (both “full” and “dark-only” runs, as well as for other specific cases, as discussed in the main text; also c.f. Tab. 1). The residues are shown in Fig. B1 as a function of redshift and cell size. As the counting cells are allowed to intersect, they form a statistical ensemble which is not entirely independent. Even if the cells were adjacent, objects belonging to nearby cells would be correlated. Hence, given that the long range nature of the gravitational clustering, all cells are correlated in

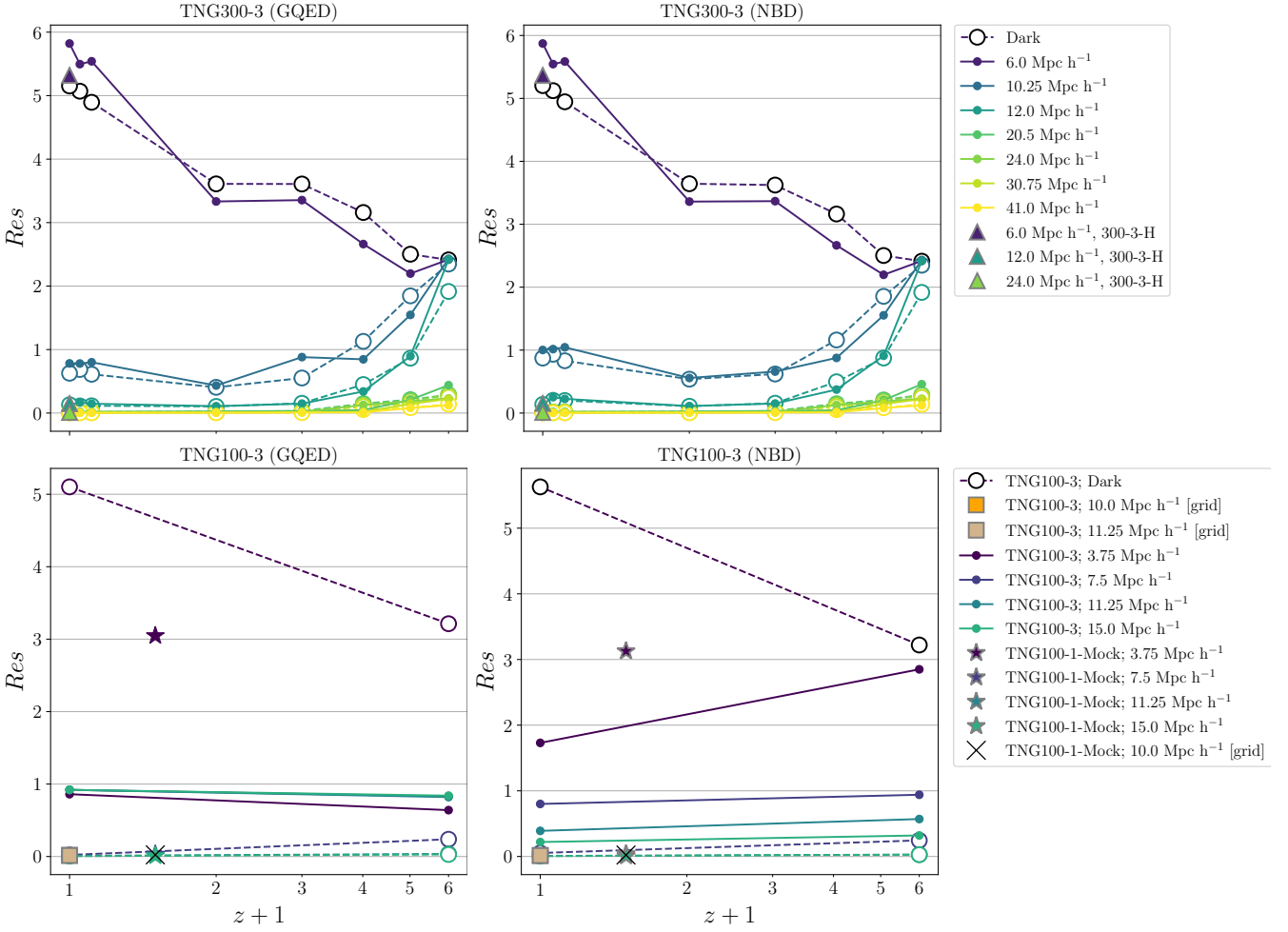


**Figure B1.** (Color online). Residual 2-norms as a function of redshift, for the GQED (left panels) and the NBD (right panels) fits respectively; the TNG300 results are at top panels and the TNG100 results are in the bottom panels.

different degrees. In any case, the higher the number of cells in the ensemble used for the CiC computation, the better the statistics will be concerning the resulting form of  $f_V(N)$ . For the analysis of the goodness of the fitting models, we did not evaluate the  $\chi^2$  estimates due to cell correlations; we use residual 2-norms of the fits, namely:

$$Res = \sum_{N_0}^{N_{\max}} [f_V(N)_{\text{sim}} - f_V(N)_{\text{theo}}]^2, \quad (\text{B1})$$

where  $N_0 \equiv (N = 0)$  and  $N_{\max}$  is the largest number of galaxies in a cell.

We found that the residues (for both GQED and NBD models) are larger for smaller comoving cell sizes, specially for the smallest size, in both TNG100-3 and TNG300-3 runs. The “dark-only” TNG100-3 run shows a larger residue than in its “full” counterpart for the smallest cell. In the TNG300-3 runs, except for the smallest cell, residues tend to increase for higher redshifts (but this trend is inverted for the smallest cell). The TNG300-3-H case, in which twice of initial counting cells was used (c.f. App. A), shows smaller residues (relative to each cell size) than the TNG300-3 runs at  $z = 0$ , with no visible discrepancies in residues for the cell size of 12 [Mpc h<sup>-1</sup>], which has shown an apparent excess in the parameter values at that size, as discussed in the main text. Overall, both GQED and NBD models show similar residues, with the quality of fits being only slightly better for the GQED models in most cases, but the present results are not definite in this regard.

## REFERENCES

- Abazajian K. N., et al., 2009, *ApJS*, **182**, 543
- Ahmad F., Saslaw W. C., Bhat N. I., 2002, *ApJ*, **571**, 576
- Alimi J.-M., et al., 2012, DEUS Full Observable LambdaCDM Universe Simulation: the numerical challenge ([arXiv:1206.2838](https://arxiv.org/abs/1206.2838))
- Baugh C. M., 2006, *Reports on Progress in Physics*, **69**, 3101
- Berlind A. A., Weinberg D. H., 2002, *The Astrophysical Journal*, **575**, 587
- Bernardeau F., Colombi S., Gaztañaga E., Scoccimarro R., 2002, *Phys. Rep.*, **367**, 1
- Blanton M. R., et al., 2005, *AJ*, **129**, 2562
- Carruthers P., Duong-van M., 1983, *Physics Letters B*, **131**, 116
- Croton D. J., Gao L., White S. D. M., 2007, *MNRAS*, **374**, 1303
- Desjacques V., Jeong D., Schmidt F., 2018, *Phys. Rep.*, **733**, 1
- Elizalde E., Gaztanaga E., 1992, *MNRAS*, **254**, 247
- Garcia-Quintero C., Ishak M., Fox L., Lin W., 2019, *Phys. Rev. D*, **100**, 123538
- Hurtado-Gil L., Martínez V. J., Arnalte-Mur P., Pons-Bordería M.-J., Pareja-Flores C., Paredes S., 2017, *A&A*, **601**, A40
- Itoh M., Inagaki S., Saslaw W. C., 1988, *ApJ*, **331**, 45
- Itoh M., Inagaki S., Saslaw W. C., 1993, *ApJ*, **403**, 476
- Jones E., Oliphant T., Peterson P., et al., 2001, SciPy: Open source scientific tools for Python, <http://www.scipy.org/>
- Kim J., Park C., Choi Y.-Y., 2008, *The Astrophysical Journal*, **683**, 123
- Kim J., Changbom P., L’Huillier B., Hong S. E., 2015, *Journal of The Korean Astronomical Society*, **48**, 213
- Leicht O., Uhlemann C., Villaescusa-Navarro F., Codis S., Hernquist L., Genel S., 2019, *MNRAS*, **484**, 269
- Li C., White S. D. M., 2009, *MNRAS*, **398**, 2177
- Marinacci F., et al., 2018, *MNRAS*, **480**, 5113
- Martizzi D., et al., 2019, *MNRAS*, **486**, 3766
- Martizzi D., Vogelsberger M., Torrey P., Pillepich A., Hansen S. H., Marinacci F., Hernquist L., 2020, *MNRAS*, **491**, 5747
- McBride C., Berlind A. A., Scoccimarro R. e., 2011, *BAAS*, **43**, 249.07
- Montero-Dorta A. D., et al., 2020, *MNRAS*, **496**, 1182
- Naiman J. P., et al., 2018, *MNRAS*, **477**, 1206
- Nelson D., et al., 2018, *MNRAS*, **475**, 624
- Nelson D., et al., 2019, *Computational Astrophysics and Cosmology*, **6**, 2
- Peebles P. J. E., 1980, *The large-scale structure of the universe*. Princeton University Press
- Perlmutter S., et al., 1999, *ApJ*, **517**, 565
- Pillepich A., et al., 2018, *MNRAS*, **475**, 648
- Planck Collaboration et al., 2016, *A&A*, **594**, A13
- Python 2019, Python Language Reference, version 3.7.6, <http://www.python.org>
- Riess A. G., et al., 1998, *AJ*, **116**, 1009
- Rodriguez-Gomez V., et al., 2019, *MNRAS*, **483**, 4140
- Saslaw W. C., 1985, *Gravitational Physics of Stellar and Galactic Systems*. Cambridge, UK: Cambridge University Press
- Saslaw W. C., 1986, *ApJ*, **304**, 11
- Saslaw W. C., 2000, *The Distribution of the Galaxies*. Cambridge, UK: Cambridge University Press
- Saslaw W. C., Crane P., 1991, *ApJ*, **380**, 315
- Saslaw W. C., Fang F., 1996, *ApJ*, **460**, 16
- Saslaw W. C., Hamilton A. J. S., 1984, *ApJ*, **276**, 13
- Sheth R. K., Saslaw W. C., 1996, *ApJ*, **470**, 78
- Springel V., 2010, *MNRAS*, **401**, 791
- Springel V., et al., 2018, *MNRAS*, **475**, 676
- Trujillo-Gomez S., Klypin A., Primack J., Romanowsky A. J., 2011, *The Astrophysical Journal*, **742**, 16
- Uhlemann C., et al., 2018, *MNRAS*, **473**, 5098
- Waskom M., et al., 2016, seaborn: v0.7.0 (January 2016), doi:10.5281/zenodo.45133, <https://doi.org/10.5281/zenodo.45133>
- Weinberg D. H., Davé R., Katz N., Hernquist L., 2004, *ApJ*, **601**, 1
- Wen D., Kembell A. J., Saslaw W. C., 2020, *ApJ*, **890**, 160
- Yang A., Saslaw W. C., 2011, *ApJ*, **729**, 123
- York D. G., et al., 2000, *The Astronomical Journal*, **120**, 1579

This paper has been typeset from a  $\text{\TeX}/\text{\LaTeX}$  file prepared by the author.